The Astrophysical Journal, 818:28 (17pp), 2016 February 10 doi:10.3847/0004-637X/818/1/28

GALAXY OUTFLOWS WITHOUT SUPERNOVAE

Sharanya Sur[1,2], Evan Scannapieco[2], and Eve C. Ostriker[3]
[1] Indian Institute of Astrophysics, 2nd Block, Koramangala, Bangalore 560034, India; sharanya.sur@iiap.res.in, sharanya.sur@asu.edu
[2] School of Earth and Space Exploration, Arizona State University, P.O. Box 876004, Tempe-85287, USA
[3] Department of Astrophysical Sciences, Princeton University, Princeton, NJ 08544, USA
Received 2015 May 4; accepted 2015 December 14; published 2016 February 4

ABSTRACT

High surface density, rapidly star-forming galaxies are observed to have ≈50–100 km s^{-1} line of sight velocity dispersions, which are much higher than expected from supernova driving alone, but may arise from large-scale gravitational instabilities. Using three-dimensional simulations of local regions of the interstellar medium, we explore the impact of high velocity dispersions that arise from these disk instabilities. Parametrizing disks by their surface densities and epicyclic frequencies, we conduct a series of simulations that probe a broad range of conditions. Turbulence is driven purely horizontally and on large scales, neglecting any energy input from supernovae. We find that such motions lead to strong global outflows in the highly compact disks that were common at high redshifts, but weak or negligible mass loss in the more diffuse disks that are prevalent today. Substantial outflows are generated if the one-dimensional horizontal velocity dispersion exceeds ≈35 km s^{-1}, as occurs in the dense disks that have star-formation rate (SFR) densities above ≈0.1 $M_\odot$ yr^{-1} kpc^{-2}. These outflows are triggered by a thermal runaway, arising from the inefficient cooling of hot material coupled with successive heating from turbulent driving. Thus, even in the absence of stellar feedback, a critical value of the SFR density for outflow generation can arise due to a turbulent heating instability. This suggests that in strongly self-gravitating disks, outflows may be enhanced by, but need not caused by, energy input from supernovae.

Key words: galaxies: evolution – galaxies: starburst – ISM: structure

1. INTRODUCTION

Multi-wavelength observations reveal the existence of massive, galaxy-scale outflows of multiphase material, driven from rapidly star-forming galaxies (Heckman et al. 1990; Bomans et al. 1997; Pettini et al. 2001; Weiner et al. 2009; Martin et al. 2013; Rubin et al. 2014). Such outflows are thought to play a fundamental role in galaxy evolution: enriching the intergalactic medium (Songaila & Cowie 1996; Simcoe et al. 2002; Pichon et al. 2003; Schaye et al. 2003; Ferrara et al. 2005; Scannapieco et al. 2006; Martin et al. 2010; Steidel et al. 2010), shaping the galaxy mass–metallicity relation (Dekel & Silk 1986; Tremonti et al. 2004; Erb et al. 2006; Kewley & Ellison 2008; Mannucci et al. 2010), and affecting the baryonic content and number density of dwarf galaxies (Somerville & Primack 1999; Cole et al. 2000; Scannapieco et al. 2002; Benson et al. 2003). Outflows also aid in eliminating small-scale random magnetic fields from galactic disks (Shukurov et al. 2006; Sur et al. 2007; Chamandy et al. 2014), thereby preventing the large-scale dynamo from undergoing catastrophic quenching. Yet despite their importance, understanding the dynamical and microphysical processes that control the evolution of galaxy outflows remains a challenge.

One difficulty in understanding these processes stems from the complex physics of the interstellar medium (ISM), where heating by UV photons, cosmic rays, and supernova shocks operate in combination with radiative cooling processes, leading to a multiphase, supersonic medium. Given the extremely short cooling times and the importance of small physical scales, simulations with ≈parsec resolution are required to model the multiphase gas distribution and expansion of supernova remnants directly (e.g., de Avillez & Breitschwerdt 2004; Hill et al. 2012; Hennebelle & Iffrig 2014; Girichidis et al. 2015; Kim & Ostriker 2015; Walch et al. 2015). In particular, neither the correct mass of hot gas nor the correct momentum injected to the ISM by supernovae can be captured unless both the Sedov and shell formation stages are sufficiently well resolved (Kim & Ostriker 2015). Thus, galaxy-scale numerical simulations have instead relied on a number of approximations, including temporarily lowering the densities and cooling rates of heated particles (Gerritsen & Icke 1997; Thacker & Couchman 2000; Stinson et al. 2006; Governato et al. 2007), using an empirical heating function (Mac Low et al. 1989; Mac Low & Ferrara 1999), imposing an artificial temperature floor (Suchkov et al. 1994; Tenorio-Tagle & Munoz-Tunon 1998; Fujita et al. 2004), and implementing exaggerated momentum kicks (Navarro & White 1993; Mihos & Hernquist 1994), and, in the case of feedback from active galactic nuclei, storing the energy until it is sufficient to raise the temperature of the surrounding gas above a threshold value (Dalla Vecchia & Schaye 2012).

The connection to observations is further complicated by recent claims that instead of supernovae, outflows could primarily be driven by radiation pressure on dust (Thompson et al. 2005; Hopkins et al. 2011, 2012; Murray et al. 2011) or by non-thermal pressure contributed by cosmic rays (Socrates et al. 2008; Samui et al. 2010; Uhlig et al. 2012; Booth et al. 2013; Hanasz et al. 2013; Salem & Bryan 2014). In addition, the typically high ISM Reynolds numbers of $\mathrm{Re} \approx 10^5$ or greater imply that a complete understanding of these massive outflows cannot be obtained by ignoring small-scale turbulent structures. Interestingly, using a numerical subgrid model for the unresolved turbulent velocities and length scales, Scannapieco & Brüggen (2010) showed that it was possible to produce outflows of multiphase material arising from simultaneous turbulent heating and radiative cooling in the disk. Notwithstanding the approximate nature of the scheme employed, this offers support to the standard picture

that massive, galaxy-scale outflows can indeed be produced from turbulence in the disk.

One hint as to the physics of galaxy outflows may lie in the properties of the galaxies that host them. Outflows are observed over a wide range of galaxy masses, but in a smaller range of galaxy surface densities. Large outflows are ubiquitous in galaxies in which the star-formation rate (SFR) density per unit area exceeds a critical value of $\dot{\Sigma}_\star^{\rm cr} \approx 0.1\,M_\odot\,{\rm yr}^{-1}\,{\rm kpc}^{-2}$ (Heckman 2002, 2003), while the ejection of material is more sporadic for $\dot{\Sigma}_\star < \dot{\Sigma}_\star^{\rm cr}$ values (Chen et al. 2010). Recent observations also show that disks with strong outflows are characterized by velocity dispersions between $\sigma_{\rm v}^{\rm 1D} \approx 50$–$100\,{\rm km\,s}^{-1}$ (Genzel et al. 2011; Swinbank et al. 2011). Such high velocities are difficult to obtain from supernovae acting alone, as high-resolution simulations of the ISM with a wide range of supernovae rates show that such explosions can only drive velocities to ≈10–20 km s^{-1} (Dib et al. 2006; Joung & Mac Low 2006; Joung et al. 2009; Kim et al. 2011, 2013; Shetty & Ostriker 2012; Hennebelle & Iffrig 2014; Gatto et al. 2015; Martizzi et al. 2015). Therefore, how does one account for such high-velocity dispersions in these disks?

A possible solution lies in the gravitationally driven motions that occur in high surface density disks. The Toomre stability criterion (Toomre 1964) relates the total disk surface density Σ, the epicyclic frequency κ, and the sound speed c_s in infinitesimally thin disks that are marginally unstable to axisymmetric modes as $Q \equiv \kappa\, c_s/\pi\, G\, \Sigma = 1$, where G is the gravitational constant. Allowing for non-axisymmetric instabilities, magnetic fields, and interaction with a stellar disk increases the critical Q value, while thick disk effects decrease it (e.g., Romeo 1992; Kim & Ostriker 2001, 2007; Kim et al. 2002; Romeo & Falstad 2013). In the real ISM, turbulent velocities are comparable to the thermal sound speed of the warm medium and are greater than the thermal sound speed of the cold medium. Thus, any characterization of the effective Q should depend on the total (thermal plus scale-dependent turbulent) velocity dispersion (Romeo et al. 2010; Hoffmann & Romeo 2012). In addition, ISM turbulence is driven by a combination of feedback from star formation and gravitational instabilities, and characterizing stability in realistic disks is therefore quite complex (Agertz et al. 2015). However, both Milky-Way-type galaxies simulations (Wada et al. 2002; Agertz et al. 2009, 2015) and high-redshift galaxy simulations (e.g., Immeli et al. 2004; Ceverino et al. 2010; Genel et al. 2012b, 2012a) show that at sufficiently large scales gravitational instabilities promote an increase of the velocity dispersion, σ, until

$$Q_{\rm eff} \equiv [\sigma^2 + c_s^2]^{1/2}\kappa/\pi G\Sigma \approx 1. \quad (1)$$

This implies that disks with high surface densities *must* develop significant turbulent motions even if stars are unable to stir the disks sufficiently to stabilize them, because gravitational instabilities will lead to the formation of clumps moving at typical velocities $\sigma \approx \pi\, G\, \Sigma/\kappa$.

Based on these ideas, Scannapieco et al. (2012) conducted simulations of turbulently stirred, radiatively cooled media. These simulations modeled a local patch of the galaxy as a stratified medium in which turbulence was driven at a rate that matched the overall cooling rate. At low velocity dispersions, such as occur in the Milky Way, this configuration was stable for many dynamical times. On the other hand, the critical SFR density for galaxy outflows corresponds to a gas surface density of $\Sigma_{\rm g} \approx 100\,M_\odot\,{\rm pc}^{-2}$, which, assuming typical values of $\Sigma \approx 2\,\Sigma_{\rm g}$, $c_s \approx 10\,{\rm km\,s}^{-1}$, and $\kappa^{-1} \approx 15\,{\rm Myr}$, gives one-dimensional turbulent velocity dispersion of $\sigma \approx 35\,{\rm km\,s}^{-1}$ to have $Q_{\rm eff} \approx 1$. At these high dispersions, Scannapieco et al. (2012) discovered the onset of a thermal runaway, where multiphase material moved upward from the disk and out of the simulation domain, implying the absence of a stable equilibrium beyond this critical value.

In this paper, we examine effects of turbulence in Toomre-critical disks more closely by conducting three-dimensional numerical simulations of a local patch of the ISM for a range of values of the total surface density Σ and the epicyclic frequency κ. Our goal is to better understand the varying environments in galaxies of different surface densities, and the extent to which these variations lead to the direct driving of galaxy-scale outflows and to conditions that are favorable to the driving of outflows by supernovae. Motivated by the idea that large-scale gravitational instabilities maintain a level of turbulence in which $Q_{\rm eff} \approx 1$, and that these instabilities primarily involve in-plane motions, we apply driven turbulence at a forcing level that results in a horizontal velocity dispersion

$$\sigma_{\rm H} \approx \pi\, G\, \Sigma/\kappa. \quad (2)$$

As we shall show, the horizontally driven turbulence also leads to vertical motions (at a lower amplitude), and the shocks from both horizontal and vertical motions heat the gas. Thermal pressure gradients and vertical turbulence combine to drive outflows from the disk. To focus on the driving of turbulence purely by gravitational instabilities, we do not include any vertical mechanical or thermal energy input from supernovae in this study, such that all outflows obtained represent a lower limit over which stellar processes will lead to additional contributions.

Because our study is focused on obtaining a better understanding of the role of gravitational instabilities in changing the nature of the medium in which stellar processes operate, we deliberately do not attempt to re-create a full model of the ISM, in which feedback from supernovae (Dib et al. 2006; Kim et al. 2011; Shetty & Ostriker 2012), ionization fronts (Matzner 2002; Walch et al. 2012), chemical transitions (Koyama & Inutsuka 2000; Walch et al. 2011; de Avillez & Breitschwerdt 2012), radiation pressure (Krumholz & Thompson 2012; Sales et al. 2014), cosmic rays (Zirakashvili et al. 1996; Boettcher et al. 2013; Booth et al. 2013), and magnetic fields (Gressel et al. 2008; Gent et al. 2013) all play a role. Although simulations that include this physics would be closer to real galaxies, they would also be much more difficult to interpret, as we could never be sure how to connect causes and effects unambiguously. In this sense, simulations that start from simpler initial conditions and explore the role of a few free parameters are complementary to more complex ISM simulations in the science they are able to target.

The structure of this paper is as follows. In Section 2 we discuss our numerical methodology. In Section 3 we describe our results, focusing on outflow rates and phase distribution of the gas, turbulent properties, and the cooling and free-fall times in the media. Conclusions are presented in Section 4.

2. NUMERICAL MODELING

Our simulations contain only four components: (i) the equations of compressible fluid dynamics; (ii) a continuously updated average vertical gravitational acceleration to capture the evolution of the disk scale height in response to thermal pressure and vertical turbulence; (iii) radiative cooling of atomic gas in the optically thin limit; and (iv) purely horizontally driven turbulence that approximates the impact of gravitational instabilities in a rotating disk in the absence of stellar feedback.

A self-gravitating disk with velocity dispersion σ has a scale height $H = \sigma^2/(\pi G\Sigma)$. Taking this as a characteristic turbulent forcing scale $\lambda_{\rm f}$ and assuming that the effective Toomre parameter is unity so that Equation (2) holds, we have

$$\lambda_{\rm f} \approx R \equiv \pi\, G\, \Sigma/\kappa^2, \tag{3}$$

for the turbulent *stirring* scale. In reality, power may be driven by gravitational instabilities over a range of scales and will cascade to smaller scales via nonlinear interactions. Here, we chose a characteristic spatial scale for simplicity. We note that the adopted stirring scale is comparable to the range where the turbulent power spectrum reaches its maximum in the shearing box simulations of Kim & Ostriker (2007), who found that the power is flat above $\lambda_x \approx 8\, G\, \Sigma/\kappa^2$.

The simulations were conducted with the multidimensional, grid-based (magneto)-hydrodynamic code FLASH (version 4.2; Fryxell et al. 2000). While FLASH is capable of incorporating dynamical grids of varying resolution by virtue of the adaptive mesh refinement (AMR) technique, we chose to perform our simulations on a uniform grid with the unsplit hydrodynamic solver (Lee et al. 2009, 2012) in a box of size $3R$ in the x and y directions and $-3R$ to $+3R$ in the vertical direction, where R is defined by Equation (3). We adopted a $256^2 \times 512$ grid for the majority of our simulations, and, for the purpose of a resolution study, we also conducted simulations at resolutions of $64^2 \times 128$, $128^2 \times 256$, and $512^2 \times 1024$ (see the Appendix). Furthermore, we chose periodic boundary conditions in x and y and "diode" boundary conditions in the z direction, which allow for outflows of material from the simulation domain, but prevent inflows.

The initial conditions were characterized by two free parameters: the total matter surface density, Σ, and the epicyclic frequency, κ. We further assumed that the gas surface density was given by $\Sigma_{\rm g} = f_{\rm g}\,\Sigma$, where the gas fraction, $f_{\rm g}$, was fixed at $1/2$ for all our simulations. Because we do not know a priori what vertical distribution the medium will take at late times, we adopted an initial density distribution that maintained the desired surface density and approximated the vertical distribution as an exponential profile:

$$\rho = \frac{\Sigma}{2R/C}\exp\left(\frac{-|z|}{R/C}\right)\frac{1}{1-\exp(-3C)}, \tag{4}$$

where C is a "compression" factor that relates R and the initial scale height such that $H(t=0) = R/C$, and the $1-\exp(-3C)$ ensures that the total surface density within the finite domain is equal to Σ. In the gradual course of the simulation, and in the absence of any other feedback processes, the scale height, H, the vertical velocity dispersion, σ_z, and the disk thermal structure adjusted automatically to the most compact and coldest distribution available for a given choice of Σ and κ. If the turbulent motions were isotropic and thermal pressure support were minimal, then we would expect our simulations to reach a state state density distribution similar to Equation (4) with $C \approx 1$. However, if vertical turbulent motions remain smaller than horizontal ones, as we shall see is the case, then we would expect much more compact distributions, corresponding to Equation (4) with larger C values. For the simulations presented in this paper, we have used $C = (5\text{–}7)$ at $t = 0$. In general, this is somewhat more compact than the final steady state distributions described below, but because our gas distribution collapses while the turbulence is developing, we find that smaller choices of C lead to longer delays in reaching the same quasi-steady-state. In addition, in all our simulations, we employed an ideal gas equation of state with $\gamma = 5/3$ and an atomic mass of one, an initial constant temperature of $T = 2 \times 10^5$ K, and zero initial velocities.

Because our simulations were not conducted in a shearing box in which large-scale gravitational forces are opposed by centrifugal and Coriolis forces, and because we do not incorporate sink particles to handle the collapse of Jeans-unstable gas, we cannot simply implement self-gravity in our simulations. Thus, we adopted an idealized approach. First, to include the impact of gravity on the overall vertical profile of the gas, we computed a vertical acceleration that was a time-dependent function of z, and did not depend on x and y. The time dependence ensures that the system finds its own vertical scale height in the course of the simulation, rather than having the user guess a scale height a priori, as would be the case if the user were to specify a gravitational profile at runtime. Second, we added a horizontal stochastic driving term to include the impact of large-scale horizontal turbulent motions driven by gravity.

To compute the vertical gravity, at every time step we calculated a vertical acceleration profile, $g(z)$, directly from the average vertical mass profile as

$$g(|z|) = 2\pi G \int_{-|z|}^{|z|} \left|\frac{d\Sigma}{dz}\right| dz, \tag{5}$$

where we approximate $d\Sigma/dz$ as $(1/f)d\Sigma_{\rm g}/dz$. Because this acceleration is a function of height and not of horizontal position, it does not directly drive turbulence. To implement turbulent driving as would be induced by large-scale gravitational instability, we used a version of the stirring module in FLASH, adapted from one of our recent studies (Sur et al. 2014b), which models turbulent driving random motions as a stochastic Ornstein–Uhlenbeck process (Eswaran & Pope 1988; Benzi et al. 2008). Specifically, this corresponds to a Gaussian random vector field, $\boldsymbol{F}$, with an exponential temporal correlation, $t_{\rm f}$, in the momentum equation.

We drove turbulence in the range of wavenumbers $2 \leqslant |\boldsymbol{k}|\, L/2\pi \leqslant 3$, such that the average forcing wavenumber was $k_{\rm f}\, L/2\pi \simeq 2.5$. Here $L = 3R$ is the horizontal extent of the box and the wave vector $|\boldsymbol{k}| = \sqrt{(k_x^2 + k_y^2 + k_z^2)}$. This corresponds to a turbulent driving scale

$$L_{\rm f} = 2\,\pi/k_{\rm f} = 1.2\,R. \tag{6}$$

Since we wish to restrict driving of turbulence to a two-dimensional plane (to simulate the effect of self-gravity within a disk), we modified our routines to force only the horizontal

component of the velocity. The resulting turbulent forcing is of mixed type in two dimensions. However, in three dimensions the probability distribution function of the density can depend on the nature of the driving (Federrath et al. 2008). The correlation time of turbulence, $t_{\rm f}$, was chosen to be $\approx 0.1\, t_{\rm ed}$, where

$$t_{\rm ed} = L_{\rm f}/\sigma_{\rm H} = 1.2\, \kappa^{-1}, \quad (7)$$

is the eddy turnover time. For a given value of Σ and κ, the amplitude of the forcing was adjusted to get the desired value of $\sigma_{\rm H} = \pi\, G\, \Sigma/\kappa$. Note that choosing a different value of $t_{\rm f}$ would require re-adjusting the forcing amplitude so as to obtain the correct value of $\sigma_{\rm H}$.

The majority of the energy input from turbulent driving in our simulations leaves the system through radiative cooling, as it does in a real galaxy. Following the prescription of Gray & Scannapieco (2010), we implemented atomic, ionic, and Bremsstrahlung cooling in the optically thin limit, assuming local collisional equilibrium with

$$\dot{E}_{\rm cool} = (1 - Y)(1 - Y/2)\frac{\rho \Lambda(T, Z)}{(\mu {\rm m}_p)^2}. \quad (8)$$

Here $\dot{E}_{\rm cool}$ is the radiated energy per unit mass, ρ is the density in the cell, m_p is the proton mass, Y is the helium mass fraction, μ the mean atomic mass, and $\Lambda(T, Z)$ is the cooling rate as a function of temperature and metallicity. For the cooling source terms, we implemented a sub-cycling scheme (Gray & Scannapieco 2010), such that T and $\Lambda(T, Z)$ were recalculated every time $E_{\rm cool}/E > 0.1$. This is equivalent to an integral formalism that assumes a constant density over each hydrodynamic time step (Thomas & Couchman 1992; Scannapieco et al. 2001). Furthermore, in order to help the simulations reach quasi-steady-state conditions more quickly, cooling is disabled for the first $0.5\, R/\sigma_{\rm H}$ time of the simulation to avoid excessive vertical collapse while the disk gains an initial level of turbulence.

The cooling rates were calculated using the tables compiled by Wiersma et al. (2009), making the simplifying approximation that the metallicity is always solar and that the abundance ratios of the metals always occurs in solar proportions. In the upper panel of Figure 1, we show the total radiative cooling rate as a function of the temperature. The lower panel shows the behavior of the local cooling timescale defined as the ratio of the energy per unit volume to the radiative cooling rate per unit volume

$$t_{\rm cool} \equiv 1.5 n k_{\rm B} T/(\rho\, \dot{E}_{\rm cool}) \propto \rho^{-1}, \quad (9)$$

where $k_{\rm B}$ is the Boltzmann constant and $n = \rho/\mu\, m_p$ is the number density of the gas.

Following the nomenclature introduced by Wolfire et al. (1995, 2003), much of the ISM can be described as comprised of a cold neutral medium (CNM) with $T \approx 100$ K, a warm neutral medium with temperatures in the range $T \approx 6 \times 10^3$–10^4 K, and a hot ionized medium with $T \geqslant 10^6$ K. As Figure 1 shows, we have only considered cooling in the temperature range $T \approx 10^3$–10^7 K and up to a maximum density of $n_{\rm max} = 6.0 \times 10^7\ {\rm cm}^{-3}$. We note that the colder parts of the ISM occupy a small fraction of the volume (only a few percent), and while they are important for star formation, they interact much less strongly with the hot medium than the warm gas that occupies most of the volume. Since our goal is to capture the formation of galaxy outflows which are mainly comprised of hot gas in the temperature range $T \approx 10^6$–10^7 K, to the lowest order we neglect the inclusion of the cold dense phases of the ISM in our simulations. We therefore do not include low-temperature cooling, instead placing a temperature floor at 1000 K throughout the simulations. This therefore amounts to adopting a simplified description of the multiphase ISM, which, as we shall show in later sections, is sufficient for the physical problem at hand. In a test case, we lowered the temperature floor to 300 K and found the mass outflow rates to remain unchanged (see the Appendix).

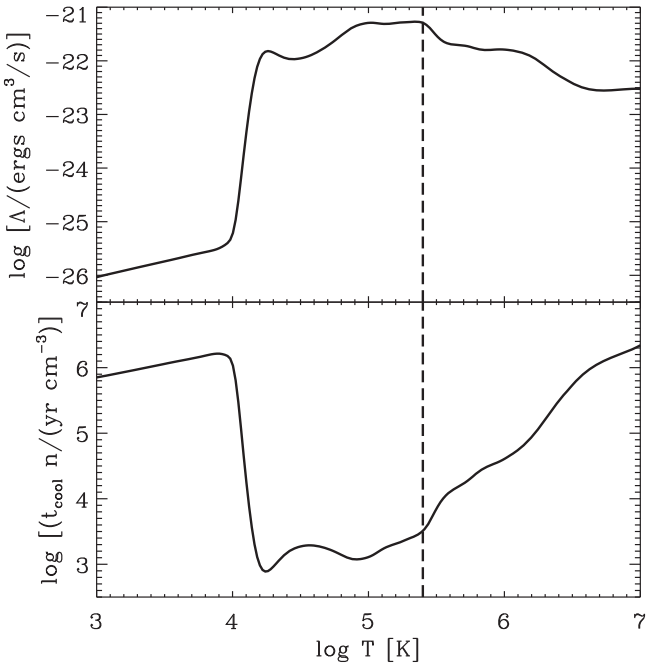

Figure 1. Total atomic, ionic, and Bremsstrahlung cooling rate (top panel) and the cooling time (bottom panel) as a function of the temperature for solar metallicity material. Note that the cooling rate drops above $T \approx 2.5 \times 10^5$ K, leading to an increase in the cooling timescale.

At temperatures $T \approx 10^4$–$10^{6.5}$ K, cooling results mainly from line emission, while cooling due to bremsstrahlung (free–free emission) becomes important at temperatures $\geqslant 10^7$ K. Below 10^4 K, collisions are not energetic enough to excite atomic transitions, leading to a drop in the cooling rate. The atomic cooling rate attains a peak value of $\Lambda \approx 10^{-21}\ {\rm erg\ cm^3\ s^{-1}}$ in the temperature range $T \approx (1 - 2.5) \times 10^5$ K. In this regime, the cooling time is roughly constant, as seen in the lower panel of the plot. The peak at $T \approx 2.5 \times 10^5$ K is dominated by line emission from metal ions, whose atomic energy levels are easily excited by collisions at this temperature. However, beyond $T \approx 2.5 \times 10^5$ K, most of the atoms become fully ionized, the effectiveness of the line cooling decreases, and the cooling rate drops, leading to a gradual increase in the cooling time. What this implies for the nature of the multiphase medium will be discussed in the next section.

3. RESULTS

3.1. Outflow Rates

As our goal is to obtain a better understanding of the turbulent ISM as a function of galaxy properties, we conducted a suite of simulations with different values of the gas surface density, $\Sigma_{\rm g}$, and the epicyclic frequency, κ. In Table 1, we present a summary of the properties of these simulations, including the run parameters ($\Sigma_{\rm g}$, κ), the key quantities for each

Table 1
Summary of the Simulation Runs at a Uniform Grid Resolution of $256^2 \times 512$

Simulation Name	Σ_g ($M_\odot$ pc^{-2})	κ^{-1} (Myr)	L_f (pc)	z_{max} (kpc)	dz (pc)	H (pc)	$\bar{\sigma}_H^{1D}$ (km s^{-1})	$\bar{\sigma}_z$ (km s^{-1})	v_{es} (km s^{-1})	$\dot{\Sigma}_g$ ($M_\odot$ yr^{-1} kpc^{-2})
S500K6.5*	500	6.5	723	1.80	7.03	7.0	68	5.0	309	0.22
S250K6.5*	250	6.5	362	0.9	3.50	9.4	35	5.5	155	0.073
S150K6.5*	150	6.5	217	0.53	2.10	17	21	6.3	92	0.04
S250K10*	250	10	856	2.13	8.32	11	50	5.5	238	0.06
S150K10*	150	10	514	1.27	4.96	20	32	6.0	142	0.03
S100K10	100	10	342	0.85	3.32	27	21	6.2	95	0.017
S150K20*	150	20	2054	5.12	20.0	22	60	5.0	285	0.03
S100K20*	100	20	1369	3.40	13.2	26	53	5.0	190	0.02
S75K20	75	20	1027	2.56	10.0	35	30	6.0	143	0.009
S50K20	50	20	685	1.70	6.64	53	21	6.3	95	0.004
S75K30	75	30	2311	5.74	22.4	33	45	5.8	214	0.005
S50K30	50	30	1541	3.83	15.0	50	30	6.0	143	0.004

Note. The different columns from the left to the right are (1) simulation name, (2) gas surface density, (3) inverse of the epicyclic frequency, (4) the horizontal forcing scale, $L_f = 1.2R$, (5) box size above the midplane, (6) the resolution, (7) vertical scale height obtained from Equation (13), (8) time-averaged, mass-weighted one-dimensional horizontal velocity dispersion, (9) time-averaged, mass-weighted vertical velocity dispersion, (10) escape velocity of the gas as defined by Equation (11), and (11) the mass-loss rate. Simulations that show persistent outflows for many eddy turnover times are marked by an asterisk.

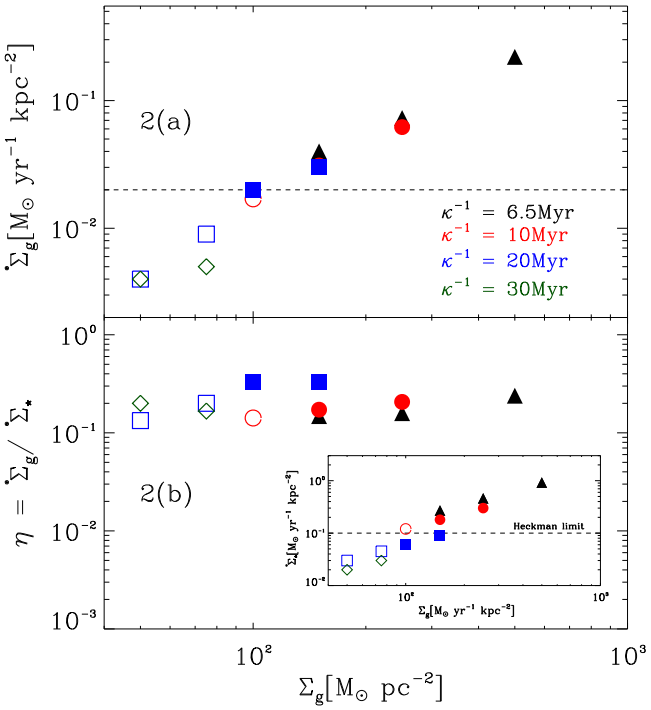

Figure 2. Upper panel shows the averaged gas mass-loss rate as a function of Σ_g for different values of κ^{-1}. Filled symbols denote runs where the computed gas mass-loss rate $\geqslant 0.02\,M_\odot$ yr^{-1} kpc^{-2} (horizontal dashed line). The lower panel shows the ratio η of the gas mass-loss rate and the SFR (where the SFR is obtained from Equation (10)). The inset panel shows the adopted variation of the SFR as a function of the gas surface density while the dashed line denotes the "Heckman limit." The filled (open) symbols in these panels follow the convention of those in panel (a).

model that can be directly derived from these parameters—the forcing scale L_f, box size above the midplane, $z_{max} = 3R$, the resolution $dz = z_{max}/256$, the horizontal velocity dispersion σ_H, and the escape velocity v_{es}, and the quantities that can only be measured from the full simulations—the vertical velocity dispersion σ_z, the scale height H, and the mass-loss rate $\dot{\Sigma}_g$. The idealized nature of our simulations enables us to probe a wide parameter space, with $\Sigma_g \in [50, 500]\,M_\odot$ pc^{-2} and $\kappa^{-1} \in [6.5, 30]$ Myr. Note, however, that for runs with $\kappa^{-1} = 30$ Myr, simulations with an initial $\Sigma_g > 75\,M_\odot$ pc^{-2} result in box sizes that are larger than the typical size of entire disk galaxies, and we have therefore chosen to omit such simulations from our study.

Our motivation for using a broad range of values is to capture the properties of high surface density galaxies over a broad range of masses and redshifts. Several attempts have been made to make predictions about the evolution of the galaxy size with redshift (see Shapley 2011; Silk & Mamon 2012; Conselice 2014 for recent reviews), and observational studies have shown that distant galaxies are more compact than those of the same mass in the nearby universe (e.g., Daddi et al. 2005; Trujillo et al. 2007; Buitrago et al. 2008; van Dokkum et al. 2010). From these studies, the dependence of galaxy size with redshift selected at a constant stellar mass can be roughly characterized as a power law of the form $R \propto (1+z)^{-\alpha}$, although Ferguson et al. (2004) find $R \propto H^{-1}(z)$ from $z \approx 1$–5, where $H(z)$ is the Hubble parameter. Assuming, for simplicity, a power-law relation between the galaxy size and redshift, it can be shown that the epicyclic frequency for a fixed mass scales as $\kappa \propto \Sigma_g^{1/2}\,(1+z)^{\alpha/2}$, while the surface density at fixed mass scales as $\Sigma_g \propto (1+z)^{2\alpha}$. These scalings imply that star-forming

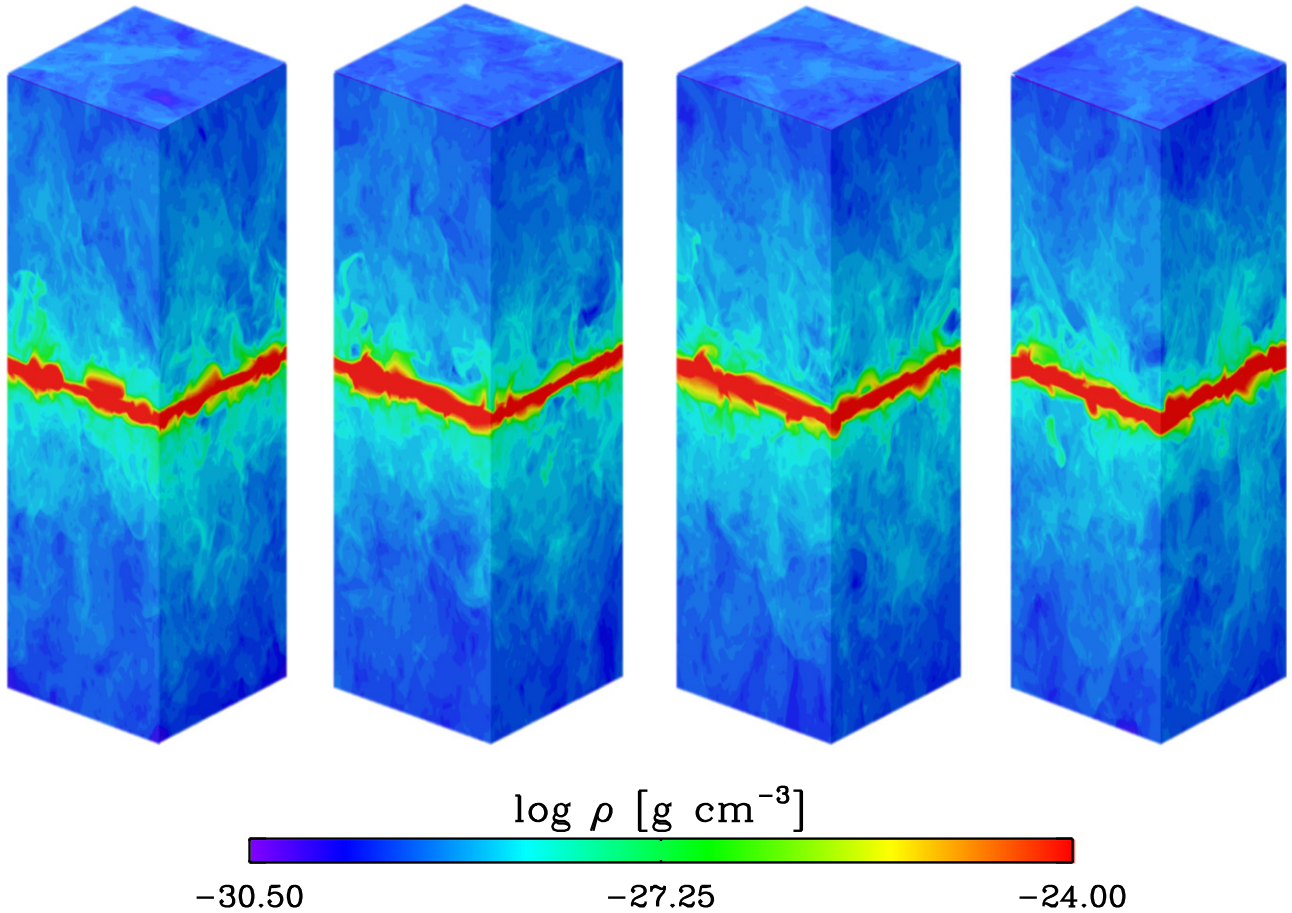

Figure 3. Three-dimensional rendering of the density in the run S250K10, showing the gradual evolution of the outflow at four different times starting from $t = 312$ to 319 Myr (left to right). For clarity of the color contrast, we have restricted the density range from log $\rho = -30.50$ to -24 [g cm^{-3}]. Plumes of gas move away from the disk midplane and leave the simulation domain through the vertical boundaries.

galaxies at higher redshifts are both more compact (i.e., have larger values of Σ_g) and are more rapidly rotating (i.e., have lower values of κ^{-1}) than their local counterparts. As we show below, this allows us to make some quantitative statements about the role of gravity-driven turbulence in powering outflows in distant galaxies. This is all the more important as the integrated SFR peaks at $z \approx 2$ (see Madau & Dickinson 2014 for a review).

In the top panel of Figure 2, we show the variation of the averaged gas mass-loss rate as a function of Σ_g for different values of κ^{-1}. The filled symbols denote runs where we find outflows with $\dot{\Sigma}_g \geqslant 0.02\, M_\odot\ \mathrm{yr}^{-1}\,\mathrm{kpc}^{-2}$, persisting over many eddy turnover times in disks. Below this threshold, outflows appear to be sporadic or absent with negligible values of $\dot{\Sigma}_g$ (denoted by open symbols), as observed in lower surface density galaxies (Chen et al. 2010). In Figure 2(b) we show the variation of the ratio of $\eta = \dot{\Sigma}_g/\dot{\Sigma}_\star$, whereas the inset figure shows the variation of the SFR alone; for this purpose, we have adopted the Kennicutt (1998) fit to the SFR density as a function of (Σ_g, κ^{-1})

$$\dot{\Sigma}_\star \approx 0.017\Sigma_g\Omega = 0.012\Sigma_g\kappa, \qquad (10)$$

where Ω is the angular velocity and in the last equality, we have assumed $\kappa = \sqrt{2}\,\Omega$, as appropriate for a flat rotation curve. The symbols (open and filled) follow the convention of those in Figure 2(a).

We recall that large-scale outflows are most likely to occur in systems in which the SFR $\dot{\Sigma}_\star \geqslant 0.1\, M_\odot\ \mathrm{yr}^{-1}\,\mathrm{kpc}^{-2}$. This implies that for each pair of values of Σ_g and κ^{-1}, massive outflows are expected for all runs except for S50K30, S75K30, S50K20, S75K20, S100K20, and S150K20. Comparing with the gas mass-loss rate plotted in Figure 2(a), we find that runs S50K30, S75K30, S50K20, and S75K20 show very weak outflows (i.e., below the threshold value of $0.02\, M_\odot\ \mathrm{yr}^{-1}\,\mathrm{kpc}^{-2}$). Among the other two runs, the mass-loss rates in S100K20 and S150K20 are on and above the threshold value, respectively. Run S100K10 lies above the "Heckman limit," but shows only a weak outflow. The ratio (η) of the gas mass-loss rate and the SFR for runs with $\kappa^{-1} = 6.5$ and 10 Myr stays nearly constant, $\eta \approx 0.1$. However, for $\kappa^{-1} = 20$ Myr, η varies weakly with Σ_g for runs both above and below the Heckman limit. The trend for $\kappa^{-1} = 30$ Myr is unclear due to our choice of simulation parameters of Σ_g.

In Figure 3, we show a three-dimensional rendering of the density at four different times, in a run with $\Sigma_g = 250\, M_\odot\ \mathrm{pc}^{-2}$ and $\kappa^{-1} = 10$ Myr. These volume renderings show the evolution of an outflow with plumes moving gradually both upwards and downwards from the midplane, eventually leaving the simulation domain. Note that the question of whether the ejected material is able to leave the simulation domain depends on whether the outflow velocity exceeds the escape velocity, which varies from simulation to simulation in our study. Specifically, given the vertical extent of the box above the

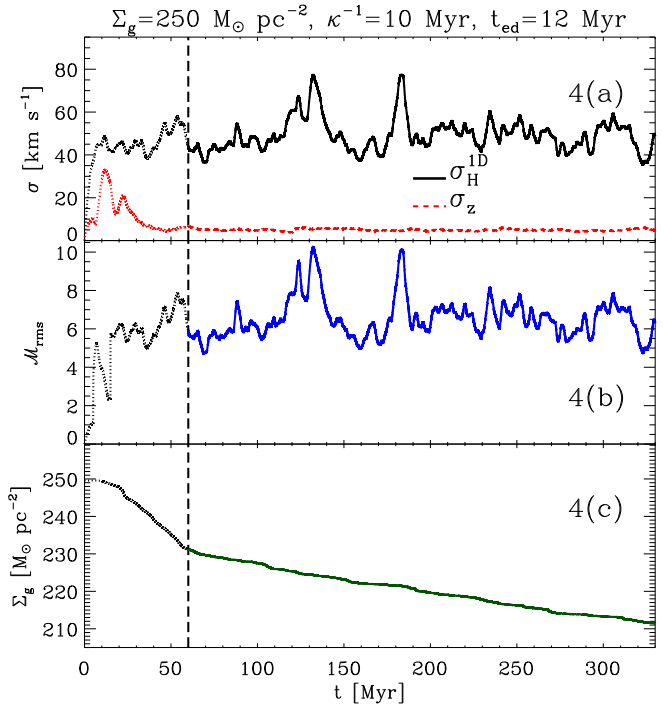

Figure 4. Time evolution of the mass-weighted, one-dimensional horizontal velocity dispersion (black, solid) and the vertical velocity dispersion (red, dashed) in panel (a), the rms Mach number (blue) in panel (b), and the gas mass surface density (dark green) in panel (c) for run SK250K10 with $\Sigma_g = 250\,M_\odot\,\mathrm{pc}^{-2}$, $\kappa^{-1} = 10\,\mathrm{Myr}$, and $t_{ed} = 12\,\mathrm{Myr}$. The dashed vertical line depicts the duration of the initial transient phase. The values of σ_H^{1D}, σ_z, and $\bar{\Sigma}_g$ presented in Table 1 are thus computed from 60 Myr onwards. Note that there is significant mass loss at times well after the initial transient phase.

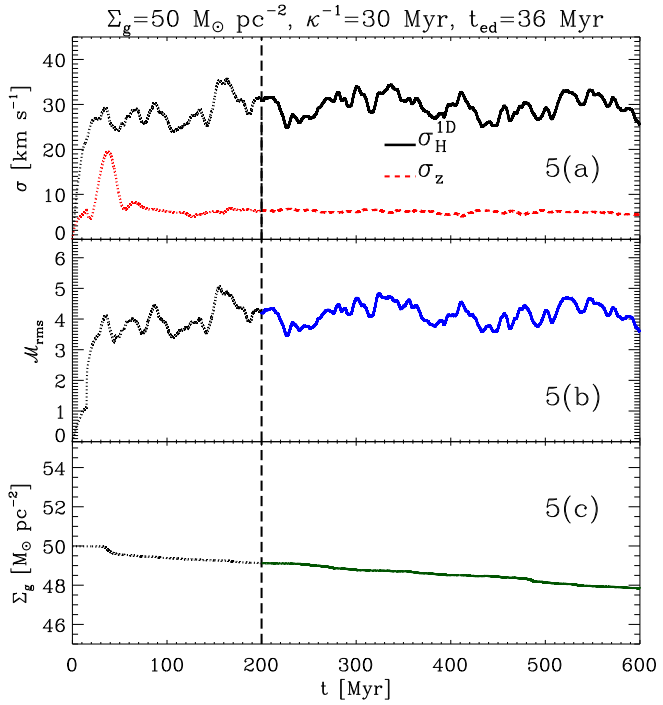

Figure 5. Same as in Figure 4 for run SK50K30 with $\Sigma_g = 50\,M_\odot\,\mathrm{pc}^{-2}$, $\kappa^{-1} = 30\,\mathrm{Myr}$, and $t_{ed} = 36\,\mathrm{Myr}$. In this case these is negligible mass loss over a 400 Myr long period.

midplane and the gas surface density, the critical velocity required to escape the gravitational potential of the host galaxy is given by

$$v_{es} = \sqrt{2\,g\,z_{max}} \approx \left(\frac{103}{\mathrm{km\ s^{-1}}}\right)\left(\frac{\Sigma_g}{100\,M_\odot\,\mathrm{pc}^{-2}}\right)^{1/2}\left(\frac{z}{\mathrm{kpc}}\right)^{1/2}, \quad (11)$$

where $g = 4\pi\,G\,\Sigma_g$ is the acceleration due to gravity (assuming $\Sigma = 2\Sigma_g$) and z_{max} is the vertical extent of the simulation volume. However, since the vertical extent is three times the driving scale R, which in turn would be related to the typical radial scale length, R_l (as $G\pi\Sigma\,R_l^2 \approx \Omega^2\,R_l$, which implies $R_l \approx \pi\,G\Sigma/\Omega^2 \approx R$) in a more complete model disk evolution, we can reasonably expect that in a real disk as material travels to heights approaching z_{max}, $g(z)$ would be falling rapidly, resulting in escape velocities similar to those in our simulations.

3.2. Time Series, Vertical Structure, and Thermal Phases

Before we delve further into the dependence of the outflows on the disk properties, we show the time evolution of two runs that illustrate the range of behaviors seen in our simulations. Figure 4 shows the evolution of S250K10, a high surface density, rapidly rotating case with $\Sigma_g = 250\,M_\odot\,\mathrm{pc}^{-2}$ and $\kappa^{-1} = 10\,\mathrm{Myr}$, and Figure 5 show the evolution of S50K30, a moderate surface density, slowly rotating case with $\Sigma_g = 50\,M_\odot\,\mathrm{pc}^{-2}$ and $\kappa^{-1} = 30\,\mathrm{Myr}$. In both figures, we plot the mass-weighted, one-dimensional horizontal velocity dispersion, $\sigma_H^{1D} = \sigma_H/\sqrt{2}$, the vertical velocity dispersion, σ_z, the mass-weighted rms Mach number, and the gas mass surface density. In both of these runs, the initial time evolution is marked by a transient phase, which lasts for 60 and 200 Myr, respectively (denoted by the dashed vertical lines), after which the system reaches a steady state. In this stage, the action of gravity in the absence of turbulent support causes the material to move downwards toward the midplane and become compressed. Then, as turbulence develops, pressure support also increases, puffing the layer back up, and causing a rapid expansion that drives a small fraction of the material out of the simulation volume. During these rearrangements, our results are strongly dependent on the particulars of our initial conditions, and so we avoid making measurements or drawing conclusions from this phase of the simulations.

On the other hand, after the initial phase has passed, the simulations settle into a quasi-steady-state that depends almost purely on Σ_g and κ. We thus evaluate the time-averaged values in Table 1 only in this quasi-steady-state. By this time, the medium in the S250K10 run settles into a roughly constant, -mass-weighted, one-dimensional horizontal velocity dispersion of $\bar{\sigma}_H^{1D} = 50\,\mathrm{km\ s^{-1}}$, while the medium in the SK50K30 run reaches $\bar{\sigma}_H^{1D} = 30\,\mathrm{km\ s^{-1}}$. While the higher surface density run is somewhat hotter than the moderate surface density case, in both runs the sound speed is well below the average velocity dispersion. In fact, the mass-weighted rms Mach number ≈6 for the higher surface density run and ≈4 in the lower surface density run, signifying the occurrence of strong shocks in both runs. Thus, although the driving in these simulations is purely horizontal, it also causes substantial pressure and density perturbations, which vary both horizontally and vertically. These in turn lead to vertical velocity fluctuations, which are

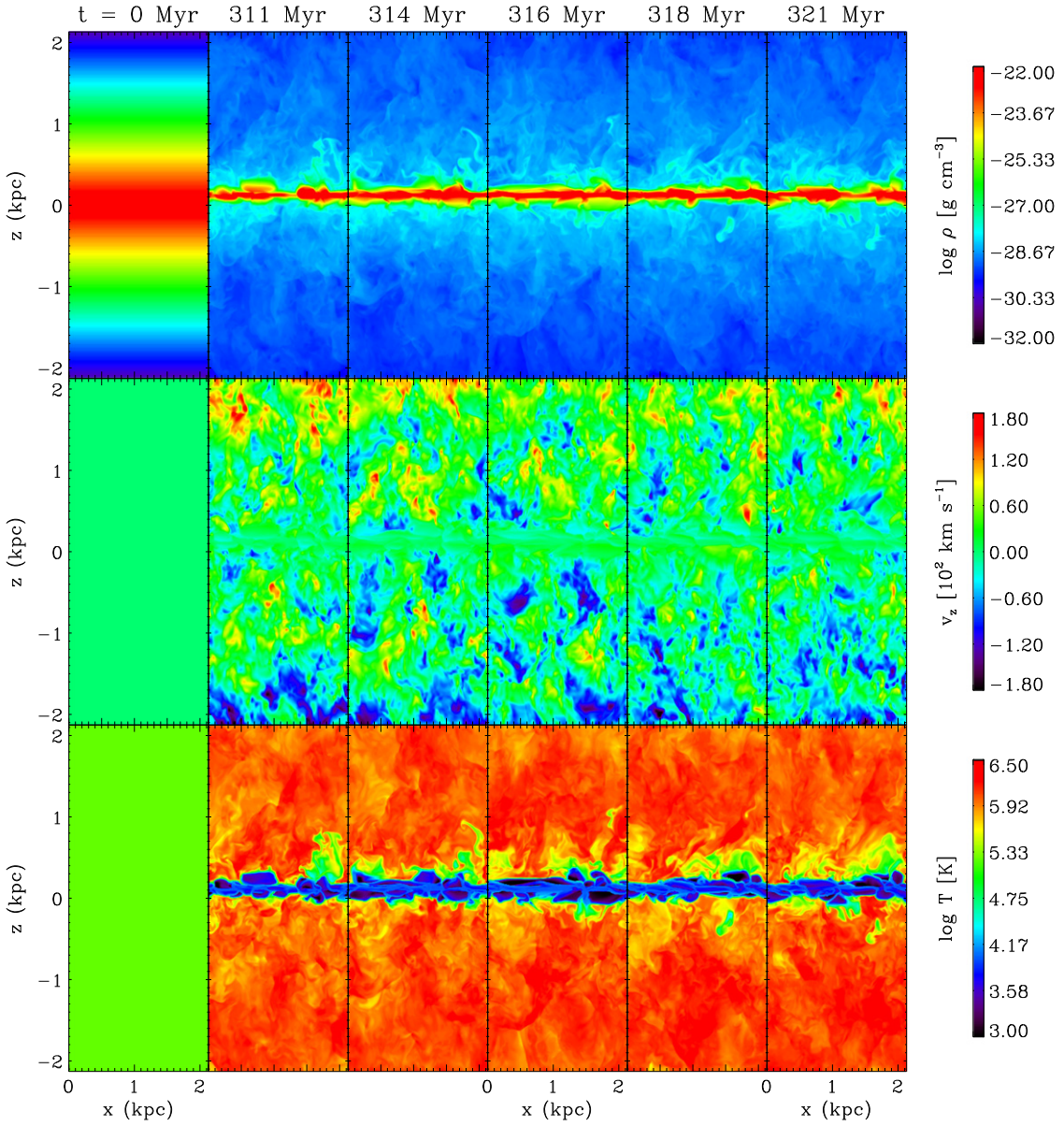

Figure 6. Two-dimensional slices in the x–z plane showing the time evolution of the logarithm of the density (upper row), the vertical component of the velocity (middle row), and the logarithm of the temperature (lower row) in a local patch of the turbulent ISM for a run with $\Sigma_g = 250\,M_\odot\,\mathrm{pc}^{-2}$, $\kappa^{-1} = 10$ Myr, and $t_{ed} = 12$ Myr. The total vertical extent of the simulation domain is $2z = 4.26$ kpc while the horizontal extent is $x = y = 2.13$ kpc.

roughly constant in time at $\bar{\sigma}_z = 5.5\,\mathrm{km\,s}^{-1}$ in the S250K10 case and $\bar{\sigma}_z = 6\,\mathrm{km\,s}^{-1}$ in the S50K30 case. This shows that the presence of supernova energy input is not required for high-density disks to develop significant turbulent motions perpendicular to the plane of the galaxy, provided large-scale self-gravitating instabilities are able to maintain horizontal motions of several tens of $\mathrm{km\,s}^{-1}$. Quite remarkably, as Table 1 shows, the value of the time-averaged, mass-weighted vertical velocity dispersion is consistently within the range from 5 to $6.3\,\mathrm{km\,s}^{-1}$ in our simulations, which we discuss in more detail below.

A closer look at these plots also reveals that for the S250K10 run, a distinct outflow occurs throughout the full quasi-steady-state evolution (see Figure 4(c)), persisting over many eddy turnover times until the simulation is terminated at $t = 330$ Myr. This is also evident from the two-dimensional x–z slices of the density, vertical component of the velocity, and temperature in Figure 6. Here we see that in the course of the evolution, the combined action of turbulent heating, radiative cooling, and gravitational collapse leads to strong density and temperature contrasts throughout the simulation. Furthermore, the slices of the density plotted in the first row of this figure, together with the vertical velocity plotted in the second row, clearly show an outflow of material.

At this point, it is worth describing in greater detail how such outflows are generated. To answer this question, we return to the total atomic, ionic, and Bremsstrahlung cooling curve in Figure 1. The temperature slices in Figure 6 show that at $t = 311$ Myr, the initial constant temperature distribution has evolved into a multiphase structure. In particular, material in certain regions close to the midplane is heated to $T \approx 10^6$ K and higher, while some patches of gas are still close to a few times 10^5 K. At the same time, Figure 1 shows that the radiative cooling rate decreases beyond $T \approx 2.5 \times 10^5$ K. This

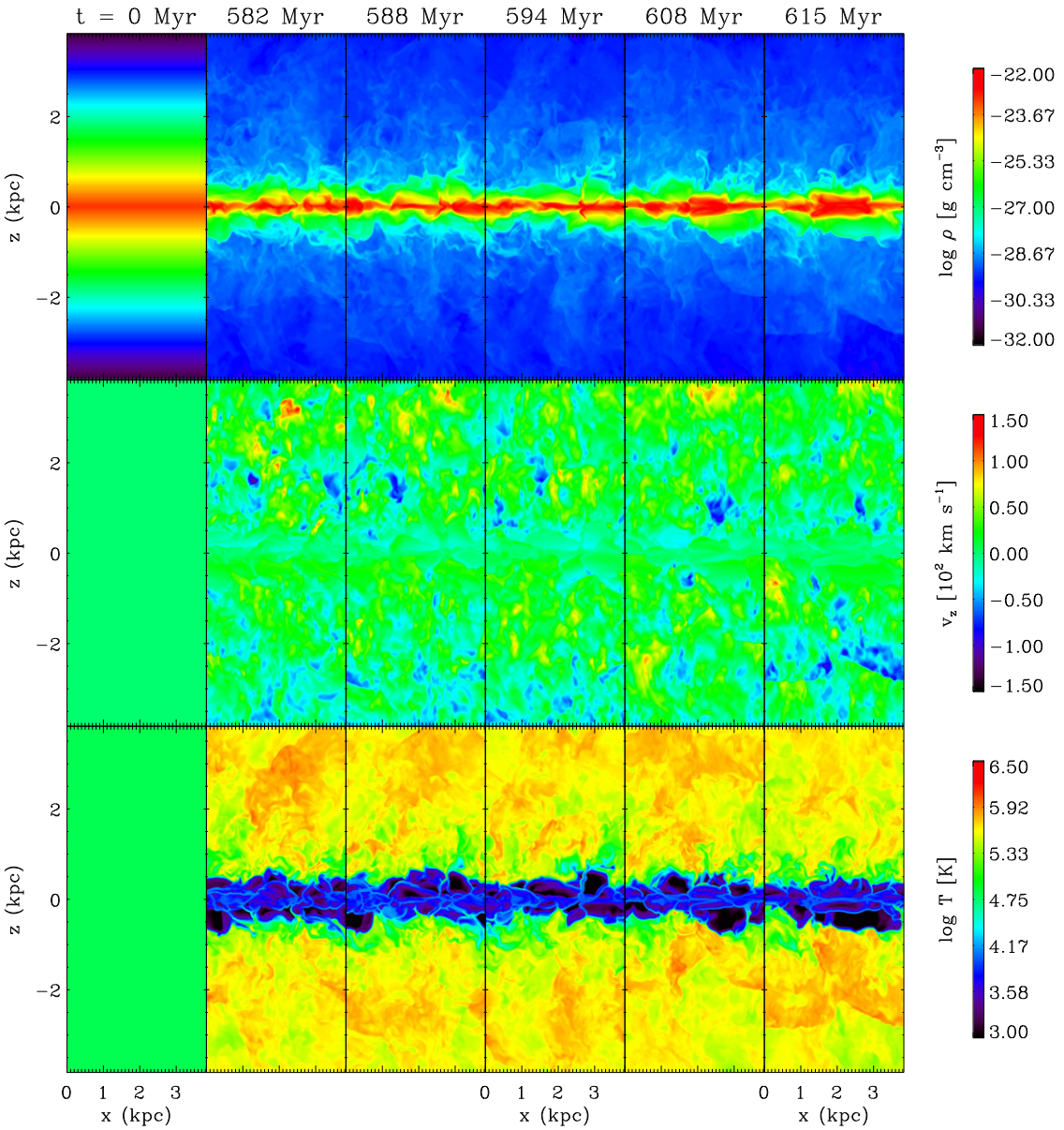

Figure 7. Two-dimensional slices in the x–z plane showing the time evolution of the logarithm of the density (upper row), the vertical component of the velocity (middle row), and the logarithm of the temperature (lower row) in a local patch of the turbulent ISM for a run with $\Sigma_g = 50\,M_\odot\,\mathrm{pc}^{-2}$, $\kappa^{-1} = 30$ Myr, and $t_{ed} = 36$ Myr. The total vertical extent of the simulation domain is $2z = 7.66$ kpc while the horizontal extent is $x = y = 3.83$ kpc.

implies that these regions would take many dynamical times to cool to the mean temperature of the medium. By then, however, successive heating resulting from turbulent driving would further heat the material.

This behavior is also expected from a linear stability analysis of a temperature perturbation in a medium in which the cooling rate per unit mass is $\propto \rho\Lambda(T)$, and the heating rate per unit mass is roughly constant, as is the case with turbulent heating (Pan & Padoan 2009). In this case, the the condition for such a perturbation to grow exponentially (at constant pressure) is simply

$$\frac{\partial \ln\Lambda}{\partial \ln T} < 1, \tag{12}$$

(Field 1965; Defouw 1970; McCourt et al. 2012). In a steadily heated, thermally unstable medium, high-density regions condense and cool, while low-density regions expand and heat. When σ is large, the temperature is high and $\partial \ln\Lambda/\partial \ln T \lesssim 0$ throughout much of the medium. This will result in an *unstable* state in which rapid, runaway heating of the hot, low-density medium will lead to the significant removal of the gas from the simulation domain (see also Scannapieco et al. 2012; Sharma et al. 2012). Figure 6 shows the continuing impact of this hot gas, which pushes its way outward both through the top and bottom boundaries.

In contrast, for a slowly rotating, moderate surface density disk, the temperature slices in Figure 7 show that the majority of the material away from the midplane is at temperatures $\leqslant 2.5 \times 10^5$ K. In this phase, $\partial \ln\Lambda/\partial \ln T \geqslant 1$ and the cooling time is roughly constant or dropping as a function of temperature, leading to a stable configuration with less significant mass loss through the vertical boundaries.

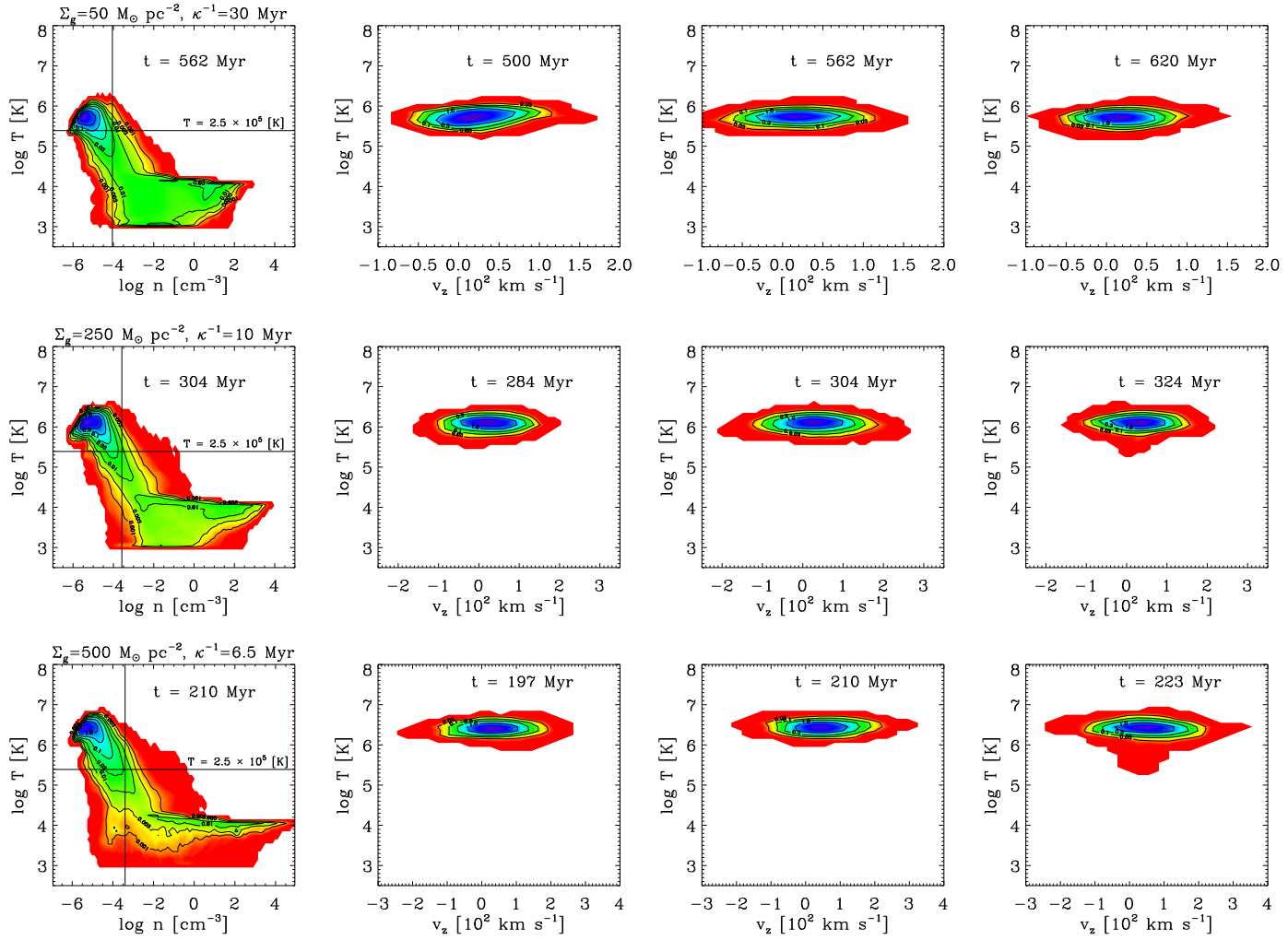

Figure 8. Volume-weighted phase diagrams of the temperature and the number density of all the gas (first column) and the mass-weighted temperature and the vertical component of the velocity PDFs of the high-latitude gas at different times (from second to the fourth column) for runs S50K30 with $\sigma_{\rm H}^{\rm 1D} = 30$ km s^{-1} and $v_{\rm esc} = 143$ km s^{-1} (top row), S250K10 with $\sigma_{\rm H}^{\rm 1D} = 50$ km s^{-1} and $v_{\rm esc} = 238$ km s^{-1} (middle row), and S500K6.5 with $\sigma_{\rm H}^{\rm 1D} = 68$ km s^{-1} $v_{\rm esc} = 309$ km s^{-1} (bottom row). The T–n phase diagrams show $\log_{10}$ contours of the probability density function, computed over the entire simulation domain, and normalized to 1 when integrated over $\ln T$ and $\ln n$. The T–v_z phase plots show $\log_{10}$ contours of the probability density function, computed over the range ($z_{\rm max}/2$–$z_{\rm max}$) for each of the three runs, and normalized to 1 when integrated in $\ln T$ and v_z in km s^{-1}. In all panels two contour lines are plotted per decade.

Such multiphase outflowing material is also detected in observed high surface density starbursting galaxies, which contain both 10^7–10^8 K emitting material (Martin 1999; Strickland & Heckman 2007, 2009) and $\approx 10^4$ K material detectable in a variety of optical and near UV absorption and emission lines (Pettini et al. 2001; Tremonti et al. 2007). Certainly, in real galaxies, much of the hottest of these phases is in fact material from supernovae. On the other hand, the presence of $\approx 10^6$ K gas may provide pockets in which the cooling of material shocked by supernova remnants is minimal, making such galaxies particularly prone to outflows. In other words, gravitationally driven turbulence is likely to both drive a baseline outflow as well as provide an ISM distribution in which supernova driving is particularly efficient.

Figure 8 shows the phase distributions of the gas for three different runs, including the temperature-density distribution over the entire simulation volume and the temperature-velocity distribution of the gas at high latitudes. In the T–n plots, $T = 2.5 \times 10^5$ K is denoted by the horizontal line, above which the cooling rate starts to decrease. The vertical lines in the plots denote the densities at which the cooling time at $T = 2.5 \times 10^5$ K is equal to the eddy turnover time. To the left of this line and for $T > 2.5 \times 10^5$ K, the cooling time is greater than $t_{\rm ed}$, while to the right, $t_{\rm cool} < t_{\rm ed}$. In all three plots, we find the existence of a horizontal, high-density tail at $T \approx 10^4$ K, a feature commonly seen in phase diagrams in ISM simulations. In the S50K30 case, corresponding to a slowly rotating, moderate surface density galaxy, a majority of material is below the threshold temperature of 2.5×10^5 K. This run has only negligible mass loss, and the T–v_z plots show that the vertical component of the velocity corresponding to the gas near the top boundary is 50–100 km s^{-1}, as compared to the escape velocity of 143 km s^{-1}.

On the other hand, in both S250K10 with $\bar{\sigma}_{\rm H}^{\rm 1D} = 50$ km s^{-1} and S500K6.5 with $\bar{\sigma}_{\rm H}^{\rm 1D} = 68$ km s^{-1}, more of the low-density gas above the disk midplane is at considerably higher temperatures than the temperature at which the cooling time is equal to the eddy turnover time. Due to the longer cooling

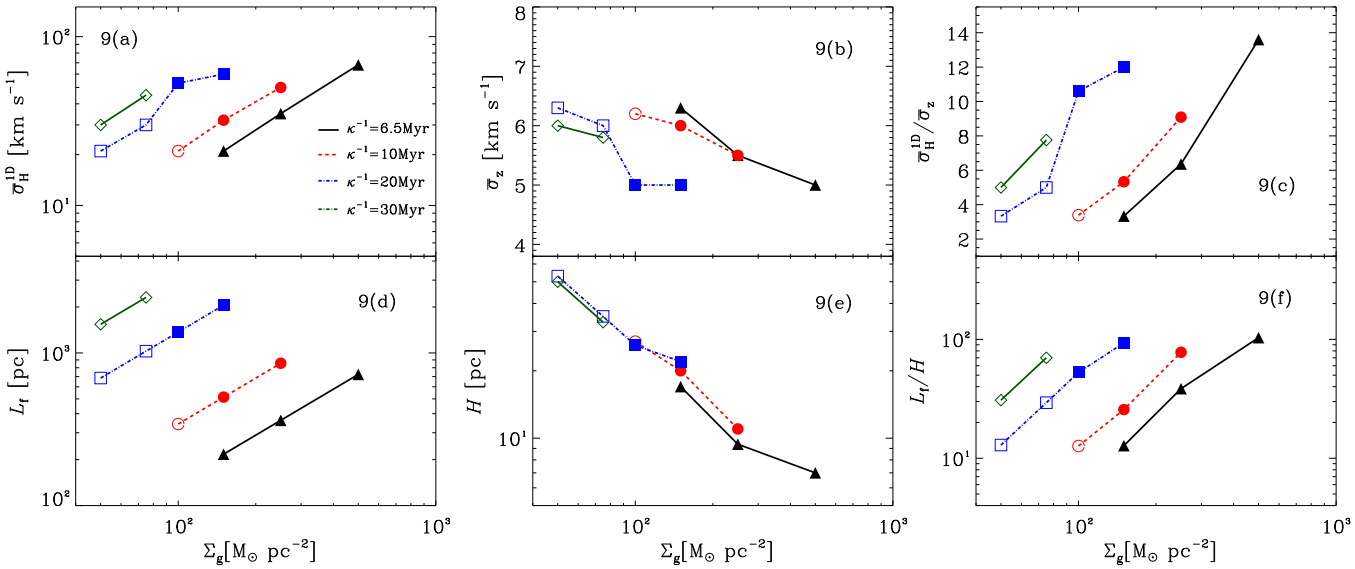

Figure 9. Different panels show the variation of the following quantities as a function of the gas surface density for different ranges of the epicyclic frequency. Panel (a)—computed one-dimensional horizontal velocity dispersion, panel (b)—vertical velocity dispersion, panel (c)—the ratio of the horizontal to the vertical velocities, panel (d)—the horizontal forcing scale, L_f, panel (e)—the scale height, H as computed in Equation (13), and the ratio of L_f/H in panel 9(f). Note that while $\sigma_H \propto \Sigma\,\kappa^{-1}$ and $L_f \propto \Sigma\,\kappa^{-2}$ are both controlled by the imposed turbulent driving, the rest of the quantities represent the natural response to horizontally driven motions.

time, this gas becomes thermally unstable and leads to a rapid, runaway heating, resulting in an eventual expulsion of the gas from the host galaxy, dragging along additional material with it. Thus, such high-density, faster spinning disks are more likely to host galaxy outflows than their slow rotating, less denser counterparts. The mass-weighted phase plots of the temperature and the vertical component of the velocity for S250K10 and S500K6.5 show that the outflowing gas is made up of a combination of phases with most of the mass in the hot phase at $T \approx 10^6$–10^7 K, which also drags along some relatively low-temperature gas as it escapes the galaxy. In both cases, the vertical velocities range from $\approx$100 km s^{-1} to close to the escape velocity, which is 238 km s^{-1} in the S250K10 case and 309 km s^{-1} in the S500K6.5 case.

3.3. Turbulent Parameters and Vertical Scale Heights

To further explore the connection between the mass-loss rate and the structure of the disk, we measured how turbulent velocities and vertical scale heights vary with our input parameters Σ_g and κ. In Figure 9, the filled (open) symbols follow the classification of disks hosting outflows above (below) 0.02 $M_\odot$ yr^{-1} kpc^{-2}, similar to those in panel (a) of Figure 2. Comparing the mass-loss rate with the one-dimensional horizontal velocity dispersion, we find that with the exception of S75K30, strong outflows are ubiquitous in systems where $\bar{\sigma}_H^{1D} \geqslant 32$ km s^{-1}. This is in agreement with earlier numerical (Scannapieco et al. 2012) and analytical predictions (Scannapieco 2013), which argued that provided turbulent velocities can be maintained above this threshold value (about 35 km s^{-1} in their paper), the material is shocked into the thermally unstable regime, leading to runaway heating and eventual expulsion from the galaxy. A compilation of a large sample of high-redshift data by Genzel et al. (2011) also shows that galaxies with $\dot{\Sigma}_\star \geqslant \dot{\Sigma}_\star^{cr}$ have $\sigma_{H\alpha}^{1D} \geqslant 35$ km s^{-1}. On the other hand, the vertical velocity dispersion varies only weakly across the entire parameter space with a mean value of 5.7 km s^{-1}.

We note here that the vertical velocity dispersion arises only in response to the horizontal turbulent motions. Even though only the horizontal turbulent velocity is stirred externally at a velocity proportional to Σ_g to model gravitational driving in an unstable disk, Figure 9(b) shows that the vertical velocity dispersion decreases only weakly with increasing gas surface density with $\sigma_z = 5.0$–6.3 km s^{-1}. Intriguingly, the small and nearly constant value of σ_z with the gas surface density is quite similar to the results from simulations in which turbulence is driven by supernovae, with a SFR set self-consistently by local gravitational collapse (Kim et al. 2011, 2013; Shetty & Ostriker 2012). However, for turbulence driven by gravitational instability, the plot of $\bar{\sigma}_H^{1D}/\bar{\sigma}_z$ in Figure 9(c) suggests that turbulent velocities become increasingly *anisotropic* with increasing gas surface density. For a constant Σ_g, the anisotropy increases for slowly rotating disks.

The variation of the imposed horizontal forcing scale, $L_f \approx R \propto \Sigma_g/\kappa^2$, is shown for reference in Figure 9(d). At constant κ^{-1}, the forcing scale is directly proportional to the gas surface density, while at constant Σ_g, slower rotating disks have a larger forcing scale. The vertical scale height, H shown in Figure 9(e) is measured directly from our simulations as the mass-weighted mean height of the gas

$$H \equiv \int_{z_{min}}^{z_{max}} |z|\rho\, dV \Big/ \int_{z_{min}}^{z_{max}} \rho\, dV. \qquad (13)$$

Since σ_z remains more or less constant with Σ_g, and $H \propto \sigma_z^2/(G\Sigma)$, this results in a decrease of the scale height with increasing Σ_g independent of the value of κ^{-1}. On the other hand, for a given value of Σ_g, the scale height is identical for different values of κ^{-1}.

Finally, we find that the ratio of the forcing scale to the disk scale height in Figure 9(f) again increases with increasing Σ_g and for a given surface density of the disk. It is also larger for more slowly rotating disks. For all models, we obtain $L_f/H > 10$. Thus, even in cases with large H, the forcing is

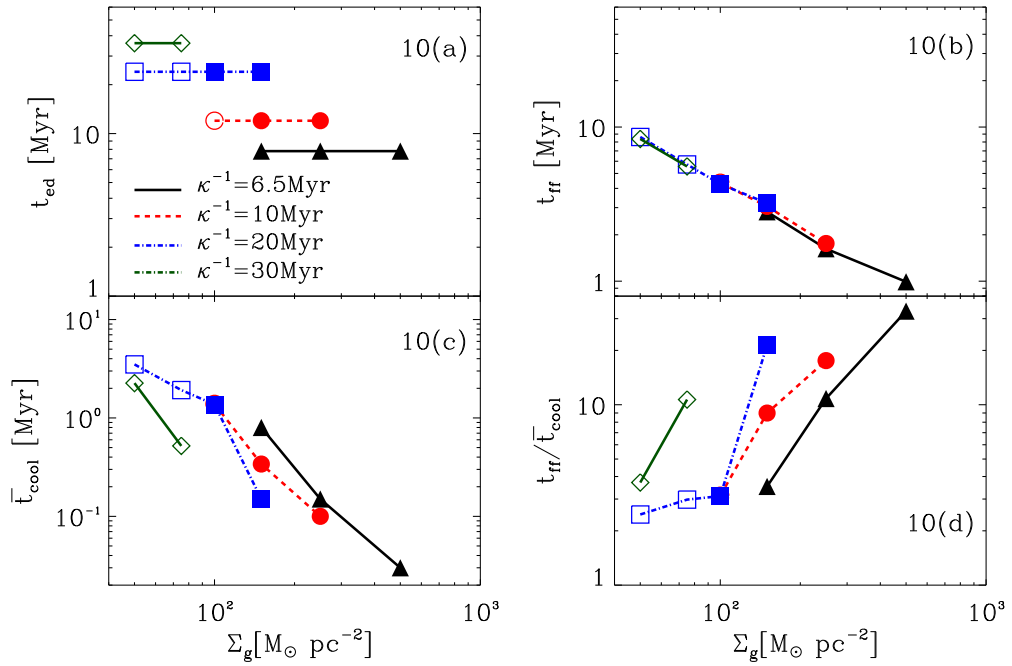

Figure 10. Variation of the eddy turnover time (panel (a)), the free-fall time (panel (b)), the average cooling time (panel (c)), and the ratio of the free-fall to the cooling time (panel (d)) with the gas surface density for simulations with different values of κ^{-1}.

still at large scales compared to the disk thickness as would be expected for gravitationally driven instabilities.

3.4. Timescales

The vertically stratified medium in our simulations is constantly heated by turbulent driving and simultaneously cooled by atomic, ionic, and Bremsstrahlung, optically thin radiative cooling. In the context of galaxy clusters, earlier works by McCourt et al. (2012) and Sharma et al. (2012) showed that such a medium only develops a multiphase structure if the free-fall timescale is longer than the average cooling time, where the local cooling time is given by Equation (9). Note, however, that McCourt et al. (2012) employed a cooling function that was dominated by thermal bremsstrahlung, while Sharma et al. (2012) included a cooling function similar to ours (Sutherland & Dopita 1993), but focused on a higher range of temperatures. More importantly, cluster turbulence is incompressible (e.g., Churazov et al. 2012; Sanders & Fabian 2012), in contrast to our simulations, in which turbulence is supersonic, and the majority of the energy is kinetic rather than thermal.

In Figure 10, we show the variation of the free-fall time, the eddy turnover time, the cooling time, and the ratio of the free-fall to the cooling timescale in our simulations as a function of surface density and rotation rate. Including constant factors, the eddy turnover time in our simulations is $t_{ed} \approx 1.2\,\kappa^{-1}$, i.e., independent of Σ. However, we must analyze our simulation results to obtain the free-fall timescale defined as

$$t_{ff} \equiv \left(\frac{H}{2\pi\ G\ \Sigma_g}\right)^{1/2} = 5.9\ \mathrm{Myr}\left(\frac{H}{100\ \mathrm{pc}}\right)^{1/2}\left(\frac{\Sigma_g}{100\ M_\odot\ \mathrm{pc}^{-2}}\right)^{-1/2}, \quad (14)$$

where we quote t_{ff} in the plane in which $z = H$, the vertical scale height defined in Equation (13). Using the values of H from Figure 9 in the above equation, we find that t_{ff} steadily decreases with Σ_g for a given value of the epicyclic frequency. Moreover, at a constant Σ_g, the free-fall timescales are similar due to identical values of the scale height. The ratio of the free-fall time to the eddy turnover time can also be written as

$$\frac{t_{ff}}{t_{ed}} = \frac{\kappa}{1.2\ \sqrt{2\pi\ G}}\left(\frac{H}{\Sigma_g}\right)^{1/2} = 0.83\left(\frac{H}{R}\right)^{1/2}, \quad (15)$$

where in the last equality we have substituted $\Sigma_g = \kappa^2\ R/2\pi\ G$, where R is the size of the eddy at the forcing scale L_f. Since the scale height $H \ll L_f$ in our simulations (see Figure 9(f)), the free-fall timescale is in general smaller than the eddy turnover time. This is also evident by comparing Figures 10(a) and (b). Equation (15) can also be expressed as the ratio of the vertical to horizontal velocity dispersion by noting that $\sigma_z \approx (2\pi\ G\ \Sigma_g\ H)^{1/2}$ and $R = \sigma_H/\kappa$ such that

$$\frac{t_{ff}}{t_{ed}} = \frac{0.8\ \sigma_z}{(2\pi\ G\ \Sigma_g)^{1/2}}\left(\frac{\kappa}{\sigma_H}\right)^{1/2} = \frac{0.8}{Q^{1/2}}\left(\frac{\sigma_z}{\sigma_H}\right), \quad (16)$$

where $Q = 2\pi\ G\ \Sigma_g/\kappa\ \sigma_H$ is the Toomre parameter. Thus, for $Q = 1$, the ratio of the free-fall to the eddy turnover time can be interpreted as the ratio of the vertical to the horizontal velocity dispersions and therefore as a measure of the isotropy of the velocities.

Using the scale height and the vertical velocity dispersion, one could construct a vertical mixing timescale, $t_{mix} = H/\sigma_z = \sigma_z/2\ \pi\ G\ \Sigma_g$, where we have substituted $H \approx \sigma_z^2/2\ \pi\ G\ \Sigma_g$. Using the values of σ_z and Σ_g from Table 1, we find that the mixing timescale is similar to the free-fall timescale with high surface density, rapidly rotating

disks having smaller mixing timescales compared to low surface density, slowly rotating disks.

In Figure 10(c) we show the mass-weighted average cooling time, $\bar{t}_{\rm cool}$, defined as the ratio of the total thermal energy to the total cooling rate. We find that the cooling times are particularly short in high surface density disks. We note here that in our simulations, the turbulence (modeling motions driven by gravitational instabilities) is converted into thermal energy and then radiated away. Thus, one could in principle also estimate the cooling time as the time taken to radiate away both the thermal energy and the kinetic energy from the system. While both these times are similar in a subsonic medium such as studied by McCourt et al. (2012) and Sharma et al. (2012), in a supersonic medium the time to radiate away the total energy would be much longer than the time to radiate only the thermal energy.

The ratio of the free-fall time to the average cooling time calculated from the thermal energy plotted in Figure 10(d) shows that $t_{\rm ff}/\bar{t}_{\rm cool} > 1$ for all the runs in this paper, even though $t_{\rm ff}/t_{\rm eddy} < 1$, meaning that material will collapse vertically faster then gravitational driving will form clumps horizontally. Thus, in agreement with the earlier results of (McCourt et al. 2012) and Sharma et al. (2012), we expect a multiphase distribution. On the other hand, as Table 1 shows, not all of these runs harbor strong outflows. Within the realm of our numerical setup, horizontal driving always allows for $t_{\rm ff}/\bar{t}_{\rm cool} > 1$ and a multiphase medium, but this is not a sufficient condition for the existence of sustainable outflows.

4. CONCLUSIONS

Global outflows occur across a wide range of galaxy masses and redshifts, and observations suggest that they are most prominent in galaxies in which the SFR density exceeds $\dot{\Sigma}_\star \geqslant 0.1\,M_\odot\,{\rm yr}^{-1}\,{\rm kpc}^{-2}$. Furthermore, recent observations show that the ISM in such galaxies has internal velocity dispersions of $\approx$50–100 km s^{-1} (Law et al. 2009; Strickland & Heckman 2009; Westmoquette et al. 2009; Green et al. 2010; Genzel et al. 2011; Swinbank et al. 2011). However, numerical simulations with supernova driving typically attain velocity dispersions of only $\approx$7–20 km s^{-1}. As current observations are unable to resolve the disk scale height or cleanly determine the orientation of random velocities with respect to the plane, it is thus possible that the large observed velocity dispersions arise not from stellar feedback but from large-scale gravitational instabilities in the disk. These will occur on scales $R \gg H$ and tap into macroscopic differences in the rotation rate and the gravitational potential, rather than nuclear processes, to drive large, anisotropic random motions.

Here we have carried out a first exploration of the possible role of gravitational instabilities in driving outflows from high surface density disk galaxies. To focus on the effect of instabilities rather than the growth and maintenance of these modes, we drive turbulence to a level expected for a Toomre-critical disk. Within this framework, we examine the role of two key parameters, namely the gas surface density, $\Sigma_{\rm g}$, and the epicyclic frequency, κ. Crucially, only the horizontal turbulence is driven, consistent with expectations for disk instabilities. The advantage of this parametrization, in which $\sigma_{\rm H} = \pi G \Sigma/\kappa$, is that we are able to control the velocity dispersion by simply adjusting the surface density of the medium. This allows us to probe a wide variety of disk conditions. Moreover as Figures 2, 9 and 10 show, our approach also enables us to probe the variation of turbulent velocities, gas mass-loss rates, and the various timescales with the gas surface density and the epicyclic frequency.

The key result arising from our study is that turbulence of the amplitude expected from gravitational instabilities can indeed drive galaxy outflows at a level $\dot{\Sigma}_{\rm g}/\dot{\Sigma}_\star \gtrsim 0.1$, even in the absence of additional energy input from supernovae. Our models show that global outflows of this kind are likely to be present in the highly compact and rapidly rotating disks that were common at high redshift, while they are more likely to be weak or completely absent in less compact and slowly rotating disks such as our Milky Way. Within the range of the parameter space of $\Sigma_{\rm g}$ and κ^{-1} that we probed, $\dot{\Sigma}_{\rm g} \geqslant 0.02\,M_\odot\,{\rm yr}^{-1}\,{\rm kpc}^{-2}$ outflows occured in galaxies where the gas surface densities exceeded $100\,M_\odot\,{\rm pc}^{-2}$ with a lower bound of $\kappa^{-1} = 20$ Myr. Interestingly, this threshold values is very close to the value of the critical SFR densities of $\dot{\Sigma}_\star > 0.1\,M_\odot\,{\rm yr}^{-1}\,{\rm kpc}^{-2}$.

Our results also indicate that outflows arise if the one-dimensional horizontal velocity dispersion exceeds a critical value of $\approx$35 km s^{-1}. We find that the vertical velocity dispersion has a mean value of 5.7 km s^{-1}, largely independent of the parameters of our simulation. Such low values are also obtained in ISM simulations where supernovae feedback is explicitly included (e.g., Shetty & Ostriker 2012; Kim et al. 2013). Furthermore, two-dimensional slices in the x–z plane show their disks to be thin and quasi-steady over many eddy turnover times. In an additional test run, we lowered the temperature floor to 300 K for the S250K10 run and found that the mass outflow rate and the estimate of the mass-weighted σ_z are similar to the estimates from the fiducial S250K10 run (see the Appendix for a comparison between the two runs). This implies that lowering the temperature floor to capture the dynamics of the cold dense medium is not crucial for outflow generation.

The occurrence of outflows in our study can be further explained from the thermodynamic properties of the ISM in these disks. As Figure 6 shows, even if one starts with a constant temperature distribution, the ISM in these galaxies soon evolves into a multiphase distribution. Certain regions attain temperatures higher than the critical temperature beyond which the radiative cooling rate progressively decreases. Over the course of the evolution, this results in a runaway arising from inefficient cooling of these hot regions coupled with successive heating from turbulent driving. The combined action of these two effects leads to the motion of the gas outward through the simulation domain. In a nutshell, the above arguments suggest that in the absence of stellar feedback, outflows from high-redshift galaxies can arise from a turbulent heating instability due to the progressive decline in the efficiency of radiative cooling beyond $T \approx 2.5 \times 10^5$ K.

As a caveat, we note that the results of this study *assume* that turbulence can be sustained at a steady level $\sigma_{\rm H} \approx \pi G \Sigma_{\rm g}/\kappa$ over many local dynamical times, via horizontal instabilities at scales $R \approx \pi G \Sigma_{\rm g}/\kappa^2$ between the disk thickness $(\sigma_z/\sigma_{\rm H})^2 R/2$ and the Toomre wavelength $4\pi R$. However, previous simulations have shown that without small-scale feedback, gravitationally unstable disks may have SFRs high enough to deplete the local gas within a few orbital times (e.g., Hopkins et al. 2011; Agertz et al. 2013). This would reduce the spatial scale ($\propto R$ if Q remains $\approx$1) of gravitational instabilities and the corresponding rotational velocity differences that these

Table 2
Study of Resolution Dependence for Run S250K10

Simulation Resolution	dz (pc)	H (pc)	$\bar{\sigma}_{\rm H}^{\rm 1D}$ (km s^{-1})	$\bar{\sigma}_{\rm z}$ (km s^{-1})	$\dot{\Sigma}_{\rm g}$ ($M_\odot$ yr^{-1} kpc^{-2})
$512^2 \times 1024$	4.16	10	54	5.5	0.062
$256^2 \times 512$	8.32	11	50	5.5	0.06
$128^2 \times 256$	16.6	14	51	5.0	0.057
$64^2 \times 128$	33.3	15.5	47	7.1	0.054

instabilities can tap, leading to lower $\sigma_{\rm H} \approx \pi\ G\ \Sigma_{\rm g}/\kappa$. Thus, a state in which high amplitude turbulence is maintained over many orbital times may require significant accretion of gas from larger scales and/or suppression of local collapse by stellar feedback. We also note here that turbulent driving as implemented in our simulations is insensitive to hot or cold gas in the sense that it is likely to drive both the high-density cold gas and the low-density hot gas in a similar fashion. However, in a realistic environment, self-gravity could drive high-density and low-density gases very differently. The resulting effect on the generation of outflows in such systems merits a careful analysis.

An important limitation of our work is the neglect of cold dense phases of the ISM. An accurate modeling of the CNM requires the inclusion of cooling due to both fine structure atomic lines and CO rotational line emission. However, this would lead to the development of small, very dense structures that would not be spatially resolved in some of our present simulations. It would be interesting to include these low-temperature processes in the cooling routines in a future study with the aim to understand its effect on the generation of galaxy outflows.

An additional issue with the simulations reported here relates the number of cells by which the length scale $l_{\rm sg} \approx c_s^2/g(z)$, corresponding to the gravity source term in the momentum equation, is resolved. Because the present simulations do not follow three-dimensional self-gravitating fragmentation at small scales, the usual Truelove criterion ($l_{\rm J} > 4\ dx$) for avoiding unphysical excitation of small-scale noise in AMR simulations does not directly apply. Here, we have only vertical gravity associated with the integrated surface density of gas, which is not substantially altered by grid scale noise. However, we note that in our simulations we only just resolve the Jeans scale for low surface density disks. Thus, fully self-gravitating simulations that seek to address the issues considered in this paper would require substantially higher resolution than we have adopted here.

Our results also raise the question of how energy input from supernovae and gravitational instabilities might work in conjunction in rapidly star-forming galaxies. The outflow rates obtained in our study should be thought of as lower limits; stellar processes may or may not lead to additional mass loss. Interestingly, the high surface density disk simulations of Wada & Norman (2007) showed that the inclusion of supernova feedback did not lead to any appreciable change in the morphology or in the density PDF (see Figures 18 and 19 in their paper) compared to the case where turbulence in the disk solely arose from gravitational instabilities. However, these simulations only spanned a region 0.32 kpc in the vertical direction which may not be sufficient to draw any immediate

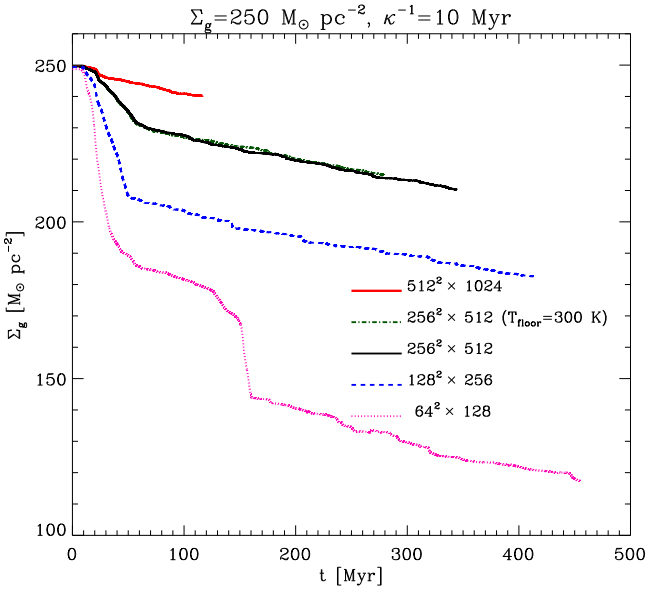

Figure 11. Time evolution of the gas surface density at four different resolutions for initial $\Sigma_{\rm g} = 250\ M_\odot$ pc^{-2}, and $\kappa^{-1} = 10$ Myr. Note that the gas mass-loss rate nears convergence from a resolution of $256^2 \times 512$, with $dz = 8.32$ pc as compared to a vertical scale height of 11 pc. It is also clear that the run with a temperature floor of 300 K has the same gas mass-loss rate as our fiducial S250K10 run.

conclusions about the combined impact of stellar feedback and gravitational instabilities. Among other questions, it will be interesting to explore how turbulent velocities resulting from the combined effect of gravitational instabilities and supernova driving scale with disk properties. Correspondingly, it will be interesting to test how SFRs differ when turbulence is driven by both supernovae and large-scale instabilities. Finally, magnetic fields are an important component of the ISM where they play a variety of roles ranging from controlling star formation, influencing turbulent mixing (Sur et al. 2014a, 2014b), to the confinement and propagation of cosmic rays. How such fields will affect the conclusions of this study is an open question. These are some of the issues we intend to address in forthcoming papers.

We thank William Gray, Christopher Matzner, Prateek Sharma, and Robert Thacker for helpful discussions and the anonymous referee for comments. S.S. and E.S. were supported by the National Science Foundation grant AST11-03608 and NASA theory grants NNX09AD106 and NNX15AK82G. E.S. gratefully acknowledges the Simons Foundation for funding the workshop *Galactic Winds: Beyond Phenomenology* which helped to inspire this work. He also gratefully acknowledges Joanne Cohn, Eliot Quataert, and the UC Berkeley Theoretical Astronomy Center, and Uroš Seljak and the Lawrence Berkeley National Lab Cosmology group for hosting him during the period when much of this work was carried out. Part of this research was carried out during the visit of E.S. and E.C.O. at the KITP in UC Santa Barbara, which is supported by the National Science Foundation under grant PHY-1125915. The work of E.C.O. on this project was supported by the National Science Foundation under grant AST-1312006. The authors thank the Texas Advanced Computing Center (TACC) at The University of Texas at Austin (URL: http://www.tacc.utexas.edu) and the Extreme Science

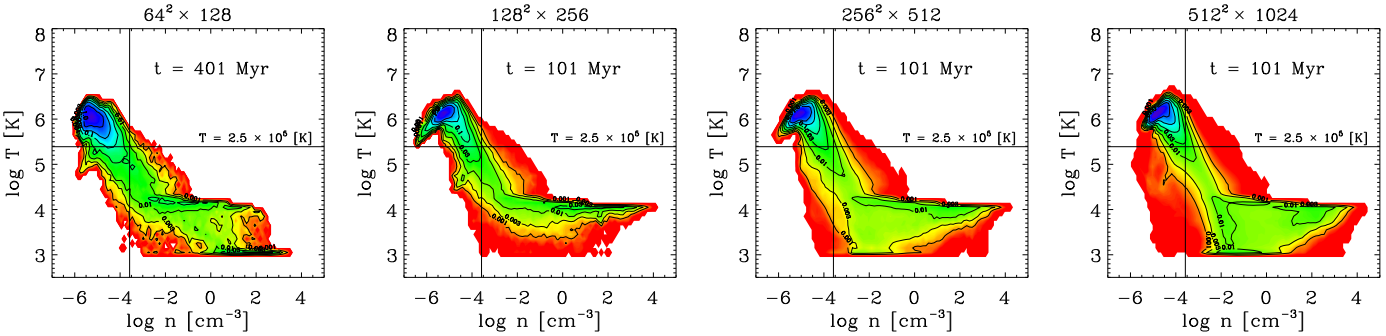

Figure 12. Volume-weighted phase diagrams of the temperature and the number density of all the gas at four different resolutions for the S250K10 run. The vertical and the horizontal lines have the same meaning as in Figure 8. At both $256^2 \times 512$ and $512^2 \times 1024$ resolutions, the phase plots show an accumulation of low-density gas at 1000 K as compared to the $128^2 \times 256$ run.

and Engineering Discovery Environment (XSEDE) for providing HPC resources via grant TG-AST140004 that have contributed to the results reported within this paper. The FLASH code is developed in part by the DOE-supported Alliances Center for Astrophysical Thermonuclear Flashes (ASC) at the University of Chicago.

APPENDIX
RESOLUTION DEPENDENCE

To explore the impact of resolution effects, we performed a resolution study for our fiducial high surface density case: S250K10, with $\Sigma_g = 250\,M_\odot$ pc^{-2} and $\kappa^{-1} = 10$ Myr. This involved a single high-resolution $512^2 \times 1024$ run, with dz half that of our standard $256^2 \times 512$ run, and two low-resolution runs with $128^2 \times 256$ and $64^2 \times 128$ cells, and dz twice and four times as large as in our standard runs, respectively. In Table 2, we show a comparison of the computed scale height, one-dimensional horizontal and vertical velocity dispersions, and gas mass-loss rate obtained in these four simulations. We also show the time evolution of Σ_g for each of the runs in Figure 11.

In all four runs, our turbulent driving results in a similar one-dimensional horizontal vertical dispersion $\approx$50 km s^{-1}. Table 2 also shows that the scale heights, vertical velocity dispersion, and gas mass-loss rate are very similar between the standard $256^2 \times 512$ run and the high-resolution $512^2 \times 1024$ run in which the scale heights were resolved by $\approx$10 and 20 cells, respectively. For the high-resolution run, the gas mass-loss rate is computed from 84 Myr to the end of the simulation. However, as evident from Figure 11, the above two runs differ in their evolution in the initial transient phase. While the $256^2 \times 512$ loses about 8.7% of its initial mass during this phase, the $512^2 \times 1024$ run loses much less mass during its initial rearrangements. Therefore, barring the estimates during the transient phase, the gas mass-loss rate is similar in both the runs. This gives us confidence that the results reported in the paper are not strongly influenced by resolution effects, and that even larger and more expensive simulations are not required to reach reliable conclusions. Moreover, by comparing the green dashed–dotted line with the black line, it appears that lowering the temperature floor to 300 K does not result in any change in the mass outflow rate. Thus, our conclusions regarding the mass outflow rates are not likely to be affected by modeling the low-temperature ISM.

Moving to the lower resolution $128^2 \times 256$ run, we find that the estimates of the horizontal velocity dispersion, vertical velocity dispersion, and gas mass-loss rate is very close to those of the two higher resolution runs. However, the estimate of the scale height falls below the resolution limit and the gas mass-loss rate in the transient phase is more than the higher resolution runs. For the lowest resolution $64^2 \times 128$ run, as Figure 11 shows, the gas mass-loss rate undergoes an extremely sharp decline for about 100 Myr followed by a steep decline from about 120–160 Myr. During this phase, the temperature also drops sharply from 1.13×10^6 K to 7.8×10^5 K, after which the system reaches a steady state. The mass-loss rate shown in the table is computed from 350 Myr onwards. In this case, the computed value of the scale height is well below the resolution limit.

In Figure 12, we show the volume-weighted T–n phase plots over the whole simulation domain at different resolutions. The phase plots are shown at 101 Myr, except for the lowest resolution run, which takes much longer to reach a steady state, and whose phase plot is shown at 401 Myr. From these diagrams it appears that the phase plots are similar for the $256^2 \times 512$ and the $512^2 \times 1024$ resolutions. However, compared to the $128^2 \times 256$ run, both of these runs show an accumulation of low-density gas at 1000 K. The $128^2 \times 256$ resolution run also shows some gas at $T = 2.5 \times 10^5$ K being dragged along with the hot outflowing gas. On the other hand, the phase plot at $64^2 \times 128$ is very different from the other three, the most significant being the accumulation of high-density gas at the temperature floor.

Thus, while the results presented here are not likely to suffer from resolution effects, they appear to be close to the lowest resolution allowable to achieve reliable results, even in the absence of additional physical processes such as stellar feedback, molecular chemistry, cosmic ray heating, and magnetohydrodynamic effects. This means that cosmological simulations that are unable to achieve $\approx$10 pc resolutions will not be able to properly handle the evolution of the ISM in high surface density galaxies similar to the S250K10 case, and may instead either over or under-represent gas mass loss depending on the particulars of the numerical method being used. Furthermore, even higher resolutions are likely to be required to model outflows from higher surface density disks with smaller vertical scale heights, even in the case without supernovae.

REFERENCES

Agertz, O., Kravtsov, A. V., Leitner, S. N., & Gnedin, N. Y. 2013, ApJ, 770, 25
Agertz, O., Lake, G., Teyssier, R., et al. 2009, MNRAS, 392, 294
Agertz, O., Romeo, A. B., & Grisdale, K. 2015, MNRAS, 449, 2156
Benson, A. J., Bower, R. G., Frenk, C. S., et al. 2003, ApJ, 599, 38
Benzi, R., Biferale, L., Fisher, R. T., et al. 2008, PhRvL, 100, 234503
Boettcher, E., Zweibel, E. G., Yoast-Hull, T. M., & Gallagher, J. S., III 2013, ApJ, 779, 12
Bomans, D. J., Chu, Y.-H., & Hopp, U. 1997, AJ, 113, 1678
Booth, C. M., Agertz, O., Kravtsov, A. V., & Gnedin, N. Y. 2013, ApJL, 777, L16
Buitrago, F., Trujillo, I., Conselice, C. J., et al. 2008, ApJL, 687, L61
Ceverino, D., Dekel, A., & Bournaud, F. 2010, MNRAS, 404, 2151
Chamandy, L., Shukurov, A., Subramanian, K., & Stoker, K. 2014, MNRAS, 443, 1867
Chen, H.-W., Helsby, J. E., Gauthier, J.-R., et al. 2010, ApJ, 714, 1521
Churazov, E., Vikhlinin, A., Zhuravleva, I., et al. 2012, MNRAS, 421, 1123
Cole, S., Lacey, C. G., Baugh, C. M., & Frenk, C. S. 2000, MNRAS, 319, 168
Conselice, C. J. 2014, ARA&A, 52, 291
Daddi, E., Renzini, A., Pirzkal, N., et al. 2005, ApJ, 626, 680
Dalla Vecchia, C., & Schaye, J. 2012, MNRAS, 426, 140
de Avillez, M. A., & Breitschwerdt, D. 2004, A&A, 425, 899
de Avillez, M. A., & Breitschwerdt, D. 2012, ApJL, 756, L3
Defouw, R. J. 1970, ApJ, 160, 659
Dekel, A., & Silk, J. 1986, ApJ, 303, 39
Dib, S., Bell, E., & Burkert, A. 2006, ApJ, 638, 797
Erb, D. K., Shapley, A. E., Pettini, M., et al. 2006, ApJ, 644, 813
Eswaran, V., & Pope, S. B. 1988, PhFl, 31, 506
Federrath, C., Klessen, R. S., & Schmidt, W. 2008, ApJL, 688, L79
Ferguson, H. C., Dickinson, M., Giavalisco, M., et al. 2004, ApJL, 600, L107
Ferrara, A., Scannapieco, E., & Bergeron, J. 2005, ApJL, 634, L37
Field, G. B. 1965, ApJ, 142, 531
Fryxell, B., Olson, K., Ricker, P., et al. 2000, ApJS, 131, 273
Fujita, A., Mac Low, M.-M., Ferrara, A., & Meiksin, A. 2004, ApJ, 613, 159
Gatto, A., Walch, S., Low, M.-M. M., et al. 2015, MNRAS, 449, 1057
Genel, S., Dekel, A., & Cacciato, M. 2012a, MNRAS, 425, 788
Genel, S., Naab, T., Genzel, R., et al. 2012b, ApJ, 745, 11
Gent, F. A., Shukurov, A., Sarson, G. R., Fletcher, A., & Mantere, M. J. 2013, MNRAS, 430, L40
Genzel, R., Newman, S., Jones, T., et al. 2011, ApJ, 733, 101
Gerritsen, J. P. E., & Icke, V. 1997, A&A, 325, 972
Girichidis, P., Walch, S., Naab, T., et al. 2015, arXiv:1508.06646
Governato, F., Willman, B., Mayer, L., et al. 2007, MNRAS, 374, 1479
Gray, W. J., & Scannapieco, E. 2010, ApJ, 718, 417
Green, A. W., Glazebrook, K., McGregor, P. J., et al. 2010, Natur, 467, 684
Gressel, O., Elstner, D., Ziegler, U., & Rüdiger, G. 2008, A&A, 486, L35
Hanasz, M., Lesch, H., Naab, T., et al. 2013, ApJL, 777, L38
Heckman, T. M. 2002, in ASP Conf. Ser. 254, Extragalactic Gas at Low Redshift, ed. J. S. Mulchaey, & J. T. Stocke (San Francisco, CA: ASP), 292
Heckman, T. M. 2003, RMxAC, 17, 47
Heckman, T. M., Armus, L., & Miley, G. K. 1990, ApJS, 74, 833
Hennebelle, P., & Iffrig, O. 2014, A&A, 570, A81
Hill, A. S., Joung, M. R., Mac Low, M.-M., et al. 2012, ApJ, 750, 104
Hoffmann, V., & Romeo, A. B. 2012, MNRAS, 425, 1511
Hopkins, P. F., Quataert, E., & Murray, N. 2011, MNRAS, 417, 950
Hopkins, P. F., Quataert, E., & Murray, N. 2012, MNRAS, 421, 3522
Immeli, A., Samland, M., Gerhard, O., & Westera, P. 2004, A&A, 413, 547
Joung, M. K. R., & Mac Low, M.-M. 2006, ApJ, 653, 1266
Joung, M. R., Mac Low, M.-M., & Bryan, G. L. 2009, ApJ, 704, 137
Kennicutt, R. C., Jr. 1998, ARA&A, 36, 189
Kewley, L. J., & Ellison, S. L. 2008, ApJ, 681, 1183
Kim, C.-G., Kim, W.-T., & Ostriker, E. C. 2011, ApJ, 743, 25
Kim, C.-G., & Ostriker, E. C. 2015, ApJ, 802, 99
Kim, C.-G., Ostriker, E. C., & Kim, W.-T. 2013, ApJ, 776, 1
Kim, W.-T., & Ostriker, E. C. 2001, ApJ, 559, 70
Kim, W.-T., & Ostriker, E. C. 2007, ApJ, 660, 1232
Kim, W.-T., Ostriker, E. C., & Stone, J. M. 2002, ApJ, 581, 1080
Koyama, H., & Inutsuka, S.-I. 2000, ApJ, 532, 980
Krumholz, M. R., & Thompson, T. A. 2012, ApJ, 760, 155
Law, D. R., Steidel, C. C., Erb, D. K., et al. 2009, ApJ, 697, 2057
Lee, D., Deane, A. E., & Federrath, C. 2009, in ASP Conf. Ser. 406, Numerical Modeling of Space Plasma Flows: ASTRONUM-2008, ed. N. V. Pogorelov et al. (San Francisco, CA: ASP), 243
Lee, D., Gopal, S., & Mohapatra, P. 2012, in ASP Conf. Ser. 459, Numerical Modeling of Space Plasma Slows (ASTRONUM 2011), ed. N. V. Pogorelov et al. (San Francisco, CA: ASP), 334
Mac Low, M.-M., & Ferrara, A. 1999, ApJ, 513, 142
Mac Low, M.-M., McCray, R., & Norman, M. L. 1989, ApJ, 337, 141
Madau, P., & Dickinson, M. 2014, ARA&A, 52, 415
Mannucci, F., Cresci, G., Maiolino, R., Marconi, A., & Gnerucci, A. 2010, MNRAS, 408, 2115
Martin, C. L. 1999, ApJ, 513, 156
Martin, C. L., Scannapieco, E., Ellison, S. L., et al. 2010, ApJ, 721, 174
Martin, C. L., Shapley, A. E., Coil, A. L., et al. 2013, ApJ, 770, 41
Martizzi, D., Faucher-Giguère, C.-A., & Quataert, E. 2015, MNRAS, 450, 504
Matzner, C. D. 2002, ApJ, 566, 302
McCourt, M., Sharma, P., Quataert, E., & Parrish, I. J. 2012, MNRAS, 419, 3319
Mihos, J. C., & Hernquist, L. 1994, ApJ, 437, 611
Murray, N., Ménard, B., & Thompson, T. A. 2011, ApJ, 735, 66
Navarro, J. F., & White, S. D. M. 1993, MNRAS, 265, 271
Pan, L., & Padoan, P. 2009, ApJ, 692, 594
Pettini, M., Shapley, A. E., Steidel, C. C., et al. 2001, ApJ, 554, 981
Pichon, C., Scannapieco, E., Aracil, B., et al. 2003, ApJL, 597, L97
Romeo, A. B. 1992, MNRAS, 256, 307
Romeo, A. B., Burkert, A., & Agertz, O. 2010, MNRAS, 407, 1223
Romeo, A. B., & Falstad, N. 2013, MNRAS, 433, 1389
Rubin, K. H. R., Prochaska, J. X., Koo, D. C., et al. 2014, ApJ, 794, 156
Salem, M., & Bryan, G. L. 2014, MNRAS, 437, 3312
Sales, L. V., Marinacci, F., Springel, V., & Petkova, M. 2014, MNRAS, 439, 2990
Samui, S., Subramanian, K., & Srianand, R. 2010, MNRAS, 402, 2778
Sanders, J. S., & Fabian, A. C. 2012, MNRAS, 421, 726
Scannapieco, E. 2013, ApJL, 763, L31
Scannapieco, E., & Brüggen, M. 2010, MNRAS, 405, 1634
Scannapieco, E., Ferrara, A., & Madau, P. 2002, ApJ, 574, 590
Scannapieco, E., Gray, W. J., & Pan, L. 2012, ApJ, 746, 57
Scannapieco, E., Pichon, C., Aracil, B., et al. 2006, MNRAS, 365, 615
Scannapieco, E., Thacker, R. J., & Davis, M. 2001, ApJ, 557, 605
Schaye, J., Aguirre, A., Kim, T.-S., et al. 2003, ApJ, 596, 768
Shapley, A. E. 2011, ARA&A, 49, 525
Sharma, P., McCourt, M., Quataert, E., & Parrish, I. J. 2012, MNRAS, 420, 3174
Shetty, R., & Ostriker, E. C. 2012, ApJ, 754, 2
Shukurov, A., Sokoloff, D., Subramanian, K., & Brandenburg, A. 2006, A&A, 448, L33
Silk, J., & Mamon, G. A. 2012, RAA, 12, 917
Simcoe, R. A., Sargent, W. L. W., & Rauch, M. 2002, ApJ, 578, 737
Socrates, A., Davis, S. W., & Ramirez-Ruiz, E. 2008, ApJ, 687, 202
Somerville, R. S., & Primack, J. R. 1999, MNRAS, 310, 1087
Songaila, A., & Cowie, L. L. 1996, AJ, 112, 335
Steidel, C. C., Erb, D. K., Shapley, A. E., et al. 2010, ApJ, 717, 289
Stinson, G., Seth, A., Katz, N., et al. 2006, MNRAS, 373, 1074
Strickland, D. K., & Heckman, T. M. 2007, ApJ, 658, 258
Strickland, D. K., & Heckman, T. M. 2009, ApJ, 697, 2030
Suchkov, A. A., Balsara, D. S., Heckman, T. M., & Leitherer, C. 1994, ApJ, 430, 511
Sur, S., Pan, L., & Scannapieco, E. 2014a, ApJL, 790, L9
Sur, S., Pan, L., & Scannapieco, E. 2014b, ApJ, 784, 94
Sur, S., Shukurov, A., & Subramanian, K. 2007, MNRAS, 377, 874
Sutherland, R. S., & Dopita, M. A. 1993, ApJS, 88, 253
Swinbank, A. M., Papadopoulos, P. P., Cox, P., et al. 2011, ApJ, 742, 11
Tenorio-Tagle, G., & Munoz-Tunon, C. 1998, MNRAS, 293, 299
Thacker, R. J., & Couchman, H. M. P. 2000, ApJ, 545, 728
Thomas, P. A., & Couchman, H. M. P. 1992, MNRAS, 257, 11
Thompson, T. A., Quataert, E., & Murray, N. 2005, ApJ, 630, 167
Toomre, A. 1964, ApJ, 139, 1217
Tremonti, C. A., Heckman, T. M., Kauffmann, G., et al. 2004, ApJ, 613, 898
Tremonti, C. A., Moustakas, J., & Diamond-Stanic, A. M. 2007, ApJL, 663, L77
Trujillo, I., Conselice, C. J., Bundy, K., et al. 2007, MNRAS, 382, 109
Uhlig, M., Pfrommer, C., Sharma, M., et al. 2012, MNRAS, 423, 2374
van Dokkum, P. G., Whitaker, K. E., Brammer, G., et al. 2010, ApJ, 709, 1018
Wada, K., Meurer, G., & Norman, C. A. 2002, ApJ, 577, 197
Wada, K., & Norman, C. A. 2007, ApJ, 660, 276
Walch, S., Wünsch, R., Burkert, A., Glover, S., & Whitworth, A. 2011, ApJ, 733, 47
Walch, S. K., Girichidis, P., Naab, T., et al. 2015, MNRAS, 454, 238

Walch, S. K., Whitworth, A. P., Bisbas, T., Wünsch, R., & Hubber, D. 2012, MNRAS, 427, 625
Weiner, B. J., Coil, A. L., Prochaska, J. X., et al. 2009, ApJ, 692, 187
Westmoquette, M. S., Smith, L. J., Gallagher, J. S., III, et al. 2009, ApJ, 696, 192
Wiersma, R. P. C., Schaye, J., & Smith, B. D. 2009, MNRAS, 393, 99
Wolfire, M. G., Hollenbach, D., McKee, C. F., Tielens, A. G. G. M., & Bakes, E. L. O. 1995, ApJ, 443, 152
Wolfire, M. G., McKee, C. F., Hollenbach, D., & Tielens, A. G. G. M. 2003, ApJ, 587, 278
Zirakashvili, V. N., Breitschwerdt, D., Ptuskin, V. S., & Voelk, H. J. 1996, A&A, 311, 113